



HAL
open science

Luminescence dating at Border Cave: attempts, questions, and new results

Chantal Tribolo, Norbert Mercier, Charles Dumottay, Nadia Cantin, William Banks, Dominic Stratford, Paloma de la Peña, Lucinda Backwell, Lyn Wadley, Francesco D'errico

► To cite this version:

Chantal Tribolo, Norbert Mercier, Charles Dumottay, Nadia Cantin, William Banks, et al.. Luminescence dating at Border Cave: attempts, questions, and new results. *Quaternary Science Reviews*, 2022, 296, pp.107787. 10.1016/j.quascirev.2022.107787 . hal-03860975

HAL Id: hal-03860975

<https://hal.science/hal-03860975v1>

Submitted on 3 Jan 2023

HAL is a multi-disciplinary open access archive for the deposit and dissemination of scientific research documents, whether they are published or not. The documents may come from teaching and research institutions in France or abroad, or from public or private research centers.

L'archive ouverte pluridisciplinaire **HAL**, est destinée au dépôt et à la diffusion de documents scientifiques de niveau recherche, publiés ou non, émanant des établissements d'enseignement et de recherche français ou étrangers, des laboratoires publics ou privés.

1 **Luminescence dating at Border Cave: attempts, questions, and new results**

2
3 **Chantal Tribolo^{a *}, Norbert Mercier^a, Charles Dumottay^a, Nadia Cantin^a, William E. Banks^{b,c},**
4 **Dominic Stratford^d, Paloma de la Peña^{e, f, g}, Lucinda Backwell^{g, h, i}, Lyn Wadley^g, Francesco**
5 **d’Errico^{b,i}**

6
7 ^a *Archéosciences Bordeaux, CNRS - Bordeaux Montaigne University, Esplanade des Antilles*
8 *33607 Pessac, France.*

9 ^b *University of Bordeaux, CNRS, MCC, PACEA, UMR 5199, Allée Geoffroy Saint Hilaire, CS 50023,*
10 *F - 33615, Pessac CEDEX, Talence, France.*

11 ^c *Biodiversity Institute, University of Kansas, Lawrence, KS, 66045-7562, USA*

12 ^d *School of Geography, Archaeology and Environmental Studies, University of the*
13 *Witwatersrand, Private Bag 3, WITS, 2050, South Africa.*

14 ^e *Departamento de Prehistoria y Arqueología, Facultad de Filosofía y Letras. Campus*
15 *Universitario de Cartuja s/n, 18071. Universidad de Granada, Spain.*

16 ^f *McDonald Institute for Archaeological Research, University of Cambridge, Downing Street,*
17 *Cambridge CB2 3ER, United Kingdom.*

18 ^g *Evolutionary Studies Institute, University of the Witwatersrand, Private Bag 3, WITS, 2050,*
19 *South Africa.*

20 ^h *Centre of Exploration for the Deep Human Journey, University of the Witwatersrand, Private*
21 *Bag 3, WITS, 2050, South Africa.*

22 ⁱ *Instituto Superior de Estudios Sociales (ISES-CONICET), San Lorenzo 429, San Miguel de*
23 *Tucumán, CP4000, Tucumán, Argentina.*

24 ^j *Centre for Early Sapiens Behaviour, Øysteinsgate 3, Postboks 7805, 5020, University of*
25 *Bergen, Norway.*

26
27 * Corresponding author: ctribolo@u-bordeaux-montaigne.fr

28
29
30 **Abstract**

31
32 Border Cave hosts a rare Middle and Early Later Stone Age sequence of deposits that extends as far
33 back as ca. 250 thousand years (ka). The site’s chronology has been built mainly on Electron Spin
34 Resonance (ESR) ages obtained from teeth, conducted at the end of the 1990s, and on radiocarbon

35 dating for the more recent layers. In order to refine the sequence's chronology, several materials were
36 selected for luminescence dating, including 34 siliceous lithic artefacts, and quartz and feldspar grains
37 extracted from 10 sediment samples. Since the radioisotopic contents of the cave sediments are
38 abundant in the volcanoclastic host rock (about 2% K, 10 ppm ²³²Th, 2 ppm ²³⁸U in the sediments) and
39 the ages for the lower layers are over 40 ka, high (> 150 Gy) equivalent doses (De) were expected for
40 most samples. The saturated thermoluminescence (TL) signals of the lithic artefact samples suggested
41 either that they had not been heated in the past, or that they were already too old to be dated. The
42 presence in the sediments of 40 - 63 µm quartz grains dominated by the fast Optically Stimulated
43 Luminescence (OSL) component and with apparent high D₀ values (200 - 1000 Gy) suggested, *a priori*,
44 that they could be appropriate for measuring high De_s. However, a systematic drop of the De values
45 for these high D₀ grains was observed and could not be fully understood and corrected accordingly.
46 The recently proposed pIT protocol, together with a global growth curve (GGC) approach, was applied
47 to 63 - 80 µm feldspar grains extracted from the sediment samples. The data suggest that the IR225
48 signal was likely not fully bleached at the time of deposition. Nonetheless, two age estimates, assumed
49 to bracket the target age, have been calculated for each sample. These estimates are consistent with
50 the previous ESR ages and the ESR/C14-based Bayesian models. Further improvements can be
51 considered in the future with the pIT - GGC method, which would allow both increased accuracy and
52 precision.

53

54 1. Introduction

55 Border Cave is one of the few sites in southern Africa that hosts a long Middle and Early Later
56 Stone Age (ELSA) sequence of deposits, and from which cultural, environmental and human remains
57 from the last 250 thousand years (ka) have been recovered. It was first excavated by Raymond Dart in
58 1934, and subsequently by Malan, Cooke and Wells in 1941-1942, following the discovery by Horton
59 of human remains during fertilizer extraction. Peter Beaumont conducted extensive excavations
60 during the 1970s and 1980s (Beaumont et al. 1978, Beaumont, 1980), followed recently by Backwell,
61 d'Errico and Wadley (Backwell et al., 2018, 2022). The sequence has been described mainly as an
62 alternating sequence of White Ash (WA) and Brown Sand (BS) deposits, numbered from 1 at the top
63 to 6 at the bottom, encompassing Iron Age, Early Later Stone Age (ELSA), Post Howiesons Poort/MSA
64 3, Howiesons Poort/MSA 2 and MSA 1 technocomplexes.

65 The sedimentary sequence of Border Cave was one of the first to be extensively dated by
66 methods based on physical or chemical processes, including radiocarbon on charcoal (mainly)
67 (Beaumont et al., 1978; Beaumont, 1980; Beaumont et al., 1992; Bird et al., 2003; Villa et al., 2012;
68 d'Errico et al., 2012), Amino Acid Racemization (AAR) on ostrich eggshells (Miller and Beaumont, 1989;
69 Miller et al., 1992; Miller et al., 1993; Miller et al., 1999), and U-series/Electron Spin Resonance (ESR)
70 on teeth (Grün et al., 1990; Grün and Beaumont, 2001; Grün et al., 2003). Radiocarbon implied that
71 the ELSA was one of the earliest currently identified in southern Africa, starting at ca. 44 ka (Beaumont
72 and Vogel, 1972; Vogel and Beaumont, 1972). This was confirmed more recently by targeted
73 radiocarbon dating of diagnostic artefacts (Villa et al., 2012; d'Errico et al., 2012). The lower part, from
74 Member 2 WA, is beyond the limit of the radiocarbon method. AAR was challenging because most of
75 the 146 tested ostrich eggshell fragments were burnt and incompatible with this method. Meanwhile
76 Members 2 BS and 2 WA, associated with MSA 3 a and b (Beaumont's attribution), were dated to 47 ±
77 5 ka, 56 ± 6 and 69 ± 7 ka with the AAR method. Members 4 BS, 4 WA and 5 BS associated with MSA 1
78 were estimated to be older than 100 ka. Grün et al. (1990, 2001, 2003) analyzed 25 bovid teeth
79 covering all members from 1 BS (ELSA) to 5 WA (MSA 1). Each tooth was subdivided into two or three
80 fragments. The ESR papers from 2001 and 2003 represent successive improvements of the

81 measurements and age calculations initiated in 1990, so here we consider only the series published in
82 2003 (Grün et al., 2003). Consistent ages were obtained for most of the Upper and Middle Pleistocene,
83 from 33 ± 1 ka to 227 ± 11 ka. A human tooth from the BC5 human mandible, discovered at the base
84 of Member 3 WA was directly dated applying U-series/ESR, and an age of 74 ± 5 ka was obtained, in
85 agreement with the ESR age for the 3 WA Member (64 ± 2 ka). A Bayesian model was then proposed
86 by Millard et al. (2006) based on the ESR data, and a Bayesian model based on the radiocarbon data
87 has also been produced (d'Errico et al., 2012).

88 J. Huxtable calculated eight thermoluminescence (TL) ages from lithics in the late 1980s and H.
89 Valladas and N. Mercier obtained 16 TL ages from 216 preselected lithics in the late 1990s (Valladas,
90 pers. comm.), which are in agreement with the other data sets, in particular with the ESR ages (Grün
91 and Beaumont (2001), and personal observation of these data). Unfortunately, none of these ages is
92 published. Despite optical dating of sediments being the most applied method to establish the
93 chronology of MSA sequences (e.g. Wadley et al., 2015), no such application has yet been published
94 for Border Cave. Here, we report one of the first complete luminescence dating studies of the Border
95 Cave sedimentary sequence, utilizing TL on lithics, and Optically Stimulated Luminescence (OSL) on
96 sedimentary quartz and feldspar grains. A brief report on the tests performed on 34 lithics can be found
97 in the Supplementary Information (Table sup.1; Fig. sup.1). We show here that only the feldspar grains
98 provide useable results. In addition, two new Bayesian models have been produced with ChronoModel
99 software from the ESR and C14 data (see Supplementary Information Section 5; Tables sup.5, sup.6A,
100 sup.6B). They are in agreement with the feldspar grains' chronology.

101

102 **2. Site and geology**

103 Here we give a brief description of the site setting and geology, which can be found in more detail
104 in Backwell et al. (2018, 2022), and Stratford et al., (2022). Border Cave is 50 m wide and 35 m long. It
105 is located 82 km west of the Indian Ocean, at 600 m.a.s.l., on a west-facing cliff of the Lebombo
106 Mountain range overlooking the Eswatini Lowveld, 500 m below. The shelter was formed by
107 differential erosion of the Lower Jurassic felsic extrusive rocks of the Jozini Formation. The two
108 volcanoclastic facies of the roof and walls of Border Cave are described as clast-supported and matrix-
109 supported breccias, which contain rhyolites, and silt- and clay-rich sandstones. The non-anthropogenic
110 components of the sediments within the cave derive mostly from the weathering of the walls and roof,
111 with additional clastic and chemical contributions from aeolian grains, and guano from bats and birds.
112 The anthropogenic component of the sediments is represented by lithic artefacts, bones, seeds, land
113 snail shells, charcoal, ash, wood, layered grass bedding, and anthropogenically introduced particles.
114 The preservation of organic material in some layers is exceptional, suggesting that the cave was, for
115 the most part, quite dry in the past. Evidence of moisture is attested by the sporadic presence of calcite
116 and gypsum, two soluble precipitate minerals, while recent stratigraphic analysis has also revealed the
117 presence of fluid interaction structures (Stratford et al., 2022). Post-depositional processes have
118 variably affected the deposits and include localized anthropogenically-induced mixing through
119 trampling or surface modification (dumping, raking of combustion features, digging of pits and
120 combustion feature bases), and geogenic processes, such as low energy run-off, mixing and reworking
121 of sediments laterally and vertically, localized spall accumulation deforming and fragmenting features,
122 and ancient and modern animal burrowing.

123 X ray diffraction (XRD) analyses were performed at the Archeosciences Bordeaux laboratory on
124 sediment samples from the upper units of the sequence (1 BS, 1 WA, 2 BS, 2 WA) (Table sup.2). They
125 clearly demonstrated the presence of quartz and calco-sodium feldspar grains, with potassium feldspar

126 in lower quantities, as well as gypsum and/or calcite. All samples, however, are dominated by zeolites,
 127 which are low-density aluminosilicate minerals formed by the devitrification of volcanic glass and
 128 derived from the breakdown of the lithologically-variable volcanoclastic rhyolites in which the shelter
 129 is hosted.

130

131 **3. Sediment samples: location and preparation**

132 Sediment samples for OSL dating were taken from the recently exposed profiles, at night, under
 133 subdued orange light, after removing the surface of the section exposed to natural light. Although the
 134 most recent excavations provide a new interpretation of the site's stratigraphy with
 135 renamed/reinterpreted layers, we attempted to identify Beaumont's members in order to link the data
 136 from the two excavations (Backwell et al., 2022; Stratford et al., 2022). Beaumont's data and in
 137 particular the location of the teeth used for obtaining the ESR data, are well known at the member
 138 level, even though their exact numerical elevations relative to the datum point are unknown. Here we
 139 present the sediment samples within the revised member boundaries along with the cultural
 140 attribution assigned by Beaumont for each one (Grün and Beaumont, 2001; Grün et al., 2003). Note,
 141 however, that these cultural attributions probably also need to be revised (de la Peña, in press).
 142 Sediment samples BDC 1, 2, 9 and 10 come from Member 2 BS, attributed to MSA 3 (Fig. 1 and Table
 143 1). Samples BDC 3 and 4 come from the lower part of Member 2 WA, also attributed to MSA 3. Sample
 144 BDC 5 is associated with the upper part of 4 BS or the lower part of 1 RGSB, so it is not clear whether
 145 it is associated with the Howiesons Poort or MSA 1. Samples BDC 6, 7 and 8 were taken respectively
 146 from Members 4 WA, 5 BS and 5 WA, all attributed to MSA 1. All samples, except for BDC 9 and 10,
 147 come from the northern area of the new excavation, in excavation 3A rear, while BDC 9 and 10 were
 148 taken at the top of the profile in the southern area (excavation 4A), from squares N103/E119 and
 149 N104/E118.

150 *Table 1. Location of the 10 sediment samples dated by OSL. The cultural attributions are those tentatively given by Grün and*
 151 *Beaumont (2001) and will be revised in the near future.*

Sample	E	N	Z	Excavation area	Member	Layer	Cultural attribution
BDC 1	119.32	109.96	104.08	northern	2 BS	Grass Mat Camilla	MSA 3
BDC 2	119.28	109.95	103.82	northern	2 BS	Yellowish Brown Caz	MSA 3
BDC 3	117.71	109.51	103.16	northern	2 WA lower	Dossy unit above combustion feature 3	MSA 3
BDC 4	118.22	109.47	103.20	northern	2 WA lower	Dossy unit above combustion feature 3	MSA 3
BDC 5	117.97	108.99	102.81	northern	1 RGSB/4 BS	Very Dark Brown Faan	HP/MSA 1
BDC 6	114.54	109.69	101.94	northern	4 WA	White Idaho	MSA 1
BDC 7	113.96	108.73	101.50	northern	5 BS	Brown John	MSA 1
BDC 8	113.95	109.49	101.43	northern	5 WA	Dark Brown Kevin	MSA 1
BDC 9	119.05	103.63	104.25	southern	2 BS	Brown Caby	MSA 1
BDC 10	118.94	104.10	104.09	southern	2 BS	Brown Caby	MSA 1

152

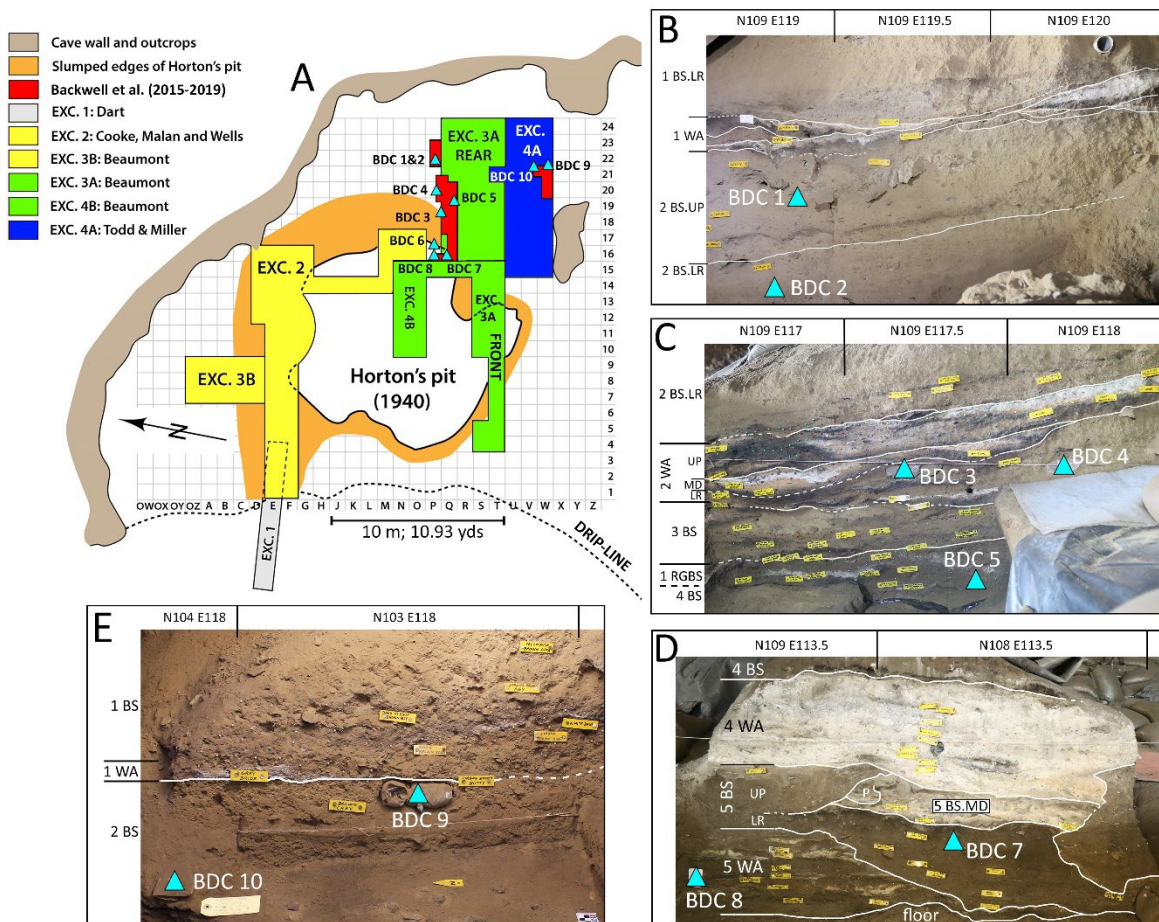
153

154

155

156

157



158

159 *Figure 1* : Location of the ten sediment samples taken for optical dating. A) shows the location of the samples in relation to
 160 the shelter, and previous and new excavation areas, and previous excavation grid established by Cooke (1941). B-E show
 161 the stratigraphic context of the samples with new grid square names (Backwell et al., 2018); B) North profile of the current
 162 excavation (northern area) showing the location of BDC1 and BDC2; C) North profile with the location of samples BDC3,
 163 BDC4 and BDC5; D) Eastern profile displaying BDC7 and 8. BDC 6 is located in 4 WA, around the left corner, in the south
 164 profile, 50 cm east of the profile face; E) Eastern profile, from the southern excavation area (by excavation 4A) displaying
 165 samples BDC9 and 10.

166

167 First, each sample was dried and sieved with 2 mm and 1 cm mesh. The >1 cm fraction was
 168 discarded. The 2 mm - 1 cm fraction and about 20 g of the <2 mm fraction were finely crushed for
 169 gamma spectrometry analyses. They were sealed in plastic containers with wax and left for at least
 170 one month before the measurements were performed. The rest of the <2 mm fraction was processed
 171 in order to extract feldspar and quartz grains. It was wet sieved at 250 and 63 μm . The 63-250 μm and
 172 <63 μm fractions were treated with HCl (10%) for carbonate removal and H₂O₂ (30%) for organic
 173 material removal. The entire <63 μm fraction was treated with H₂SiF₆ in order to retain only quartz
 174 grains, and further sieved at 20 and 40 μm . The quartz purity was checked with scanning electron
 175 microscopy-energy dispersive X-ray spectroscopy (SEM-EDS). The grains of the 63-250 μm fraction
 176 were placed successively into solutions of heteropolytungstate of sodium at densities 2.00, 2.45, 2.58,
 177 2.62, 2.72 g/cm³ in order to separate (from less dense to denser) zeolites, potassium feldspars, calco-
 178 sodium feldspars, quartz and heavy minerals. The 63-80, 80-200 and 200-250 μm granulometric
 179 fractions enriched in potassium feldspars were further separated with wet sieving and then dried. The
 180 supposedly quartz fraction (density 2.62-2.72) was completely dissolved after treatment with either

181 HF (40% for one hour, for 200-250 μm grains) or H_2SiF_6 (30%, for one week, for 100-200 μm and 63-
182 100 μm grains), suggesting that it was not quartz but denser feldspars or unusually fragile quartz.

183 The 40-63 μm quartz grains and 63-80 μm potassium feldspar grains were selected for luminescence
184 measurements.

185

186 **4. Luminescence measurement devices**

187 Most of the measurements on sedimentary quartz grains were performed on a single grain TL/OSL DA
188 20 reader (DTU Nutech, Bøtter-Jensen et al., 2000). The quartz grains were placed on discs containing
189 100 holes, each 100 μm in diameter and 100 μm deep, so that they were filled only with one or two
190 grains. Excitation was done with a 10 mW Nd: YVO₄ diode-pumped laser (532 nm) and detection was
191 done with a PDM 9107Q-AP-TTL-02 photo-multiplier tube preceded by 7 mm Hoya U340 filter (range
192 280-380 nm). The reader was equipped with a $^{90}\text{Sr}/^{90}\text{Y}$ beta source delivering about 0.10 Gy/s to the
193 quartz grains.

194 For the feldspar grains, a Lexsyg Smart reader was used. The 63-80 μm grains were attached to stainless
195 steel cups with a 5 mm silicone oil impregnated pad. Excitation was done with 850 nm LEDs and
196 detection was done with a combination of 3 mm Schott BG39 and 3.5 mm AHF Brightline HC 414/46
197 interference filter in front of a H7360-02 PM tube. The reader is equipped with a $^{90}\text{Sr}/^{90}\text{Y}$ beta source
198 delivering about 0.17 Gy/s to the grains.

199

200 **5. Dose rate: methods and results**

201 Cosmic rays, alpha and beta particles and gamma rays from natural radioisotopes present in sediments
202 and rocks, contribute to the total dose rate.

203 The calculation of the cosmic dose rate was based on the equation provided by Prescott and Hutton,
204 (1994). It takes into account the geographic coordinates of the site and the density and thickness of
205 material above the sample, the main contributor being the cave roof thickness (about 10 m, density
206 2.5 g/cm^3). The geometry of the cave was also considered, leading to a cosmic dose rate of 0.05 ± 0.01
207 Gy/ka, which was applied to all samples.

208 For estimating the gamma dose rate, *in situ* measurements were performed with dosimeters. Each one
209 contained three $\text{Al}_2\text{O}_3:\text{C}$ chips inserted in the tip of a duralumin tube (Kreutzer et al., 2018, 2020). The
210 tubes were sunk to a depth of 30 cm into the stratigraphic sections, at the locations where the
211 sediment samples had been extracted. They were left for over one year. The dosimeter associated with
212 sample BDC 1 was unfortunately lost. For each dosimeter (tube) the apparent gamma dose rate
213 increases with increased chip thickness, which was systematically recorded (Fig. sup.2), inducing a
214 scatter of about 20% (Kreutzer et al., 2020). While this scatter could be reduced with an appropriate
215 calibration that should be performed for each chip thickness, this one is not yet available, so a mean
216 calibration dose rate has been applied. The deduced gamma dose rates stand between 0.96 ± 0.15 and
217 1.59 ± 0.11 Gy/ka and are in the same range as those measured by Grün and Beaumont (2001). For
218 BDC1, the gamma dose rate was deduced from the radioisotopic contents of the sample (see below).
219 This approach is less accurate than the *in situ* measurements because it does not take into account the
220 heterogeneity of the radiation field at the centimeter scale (maximum range for gamma rays from
221 natural radioelements is about 30 cm in sediments). However, the impact of this inaccuracy on the

222 final dose rate is constrained by the fact that the gamma dose rate contributes to only about 32%
 223 (mean estimated on the other samples) of the total dose rate (Table 2).

224 *Table 2. Dose rates for the 63-80 μm feldspar grains. Beta 1 corresponds to the beta dose rate calculated from the radioisotopic*
 225 *contents of the fine (<2 mm) fraction, while beta 2 corresponds to the radioisotopic contents calculated from the total (<1 cm)*
 226 *fraction. Their mean is taken into account for the calculation of the total dose rate. The beta and alpha dose rates are corrected*
 227 *for water attenuation, taking into account the current moisture indicated in the second column (mass of water over mass of*
 228 *dry sediment). The percentage of coarse fraction in column 3 is the ratio of the mass of sediment of fraction 2 mm - 1 cm over*
 229 *the mass of sediment <1 cm. Uncertainties indicated here take into account both statistical and systematic uncertainties.*

sample	water content (%)	coarse fraction (%)	dose rates (Gy/ka)						
			cosmic	gamma	beta1	beta 2	alpha	internal	total
BDC 1	5%	16%	0.055 ± 0.005	1.33 ± 0.10	2.40 ± 0.23	2.38 ± 0.23	0.23 ± 0.03	0.30 ± 0.05	4.30 ± 0.26
BDC 2	5%	22%	0.055 ± 0.005	1.38 ± 0.14	1.61 ± 0.16	1.76 ± 0.18	0.13 ± 0.02	0.30 ± 0.05	3.55 ± 0.23
BDC 3	5%	8%	0.055 ± 0.005	0.96 ± 0.15	2.16 ± 0.21	2.17 ± 0.21	0.21 ± 0.03	0.30 ± 0.05	3.69 ± 0.26
BDC 4	5%	13%	0.055 ± 0.005	1.28 ± 0.17	2.09 ± 0.21	2.17 ± 0.21	0.19 ± 0.03	0.30 ± 0.05	3.96 ± 0.27
BDC 5	8%	9%	0.055 ± 0.005	1.19 ± 0.13	1.69 ± 0.17	1.74 ± 0.18	0.15 ± 0.02	0.30 ± 0.05	3.42 ± 0.22
BDC 6	4%	14%	0.055 ± 0.005	1.09 ± 0.06	1.32 ± 0.13	1.29 ± 0.12	0.14 ± 0.02	0.30 ± 0.05	2.89 ± 0.15
BDC 7	6%	16%	0.055 ± 0.005	1.16 ± 0.15	1.99 ± 0.20	2.02 ± 0.20	0.16 ± 0.02	0.30 ± 0.05	3.68 ± 0.26
BDC 8	7%	12%	0.055 ± 0.005	1.31 ± 0.14	1.60 ± 0.16	1.74 ± 0.18	0.14 ± 0.02	0.30 ± 0.05	3.48 ± 0.23
BDC 9	4%	25%	0.055 ± 0.005	1.59 ± 0.11	2.58 ± 0.26	2.64 ± 0.26	0.22 ± 0.03	0.30 ± 0.05	4.78 ± 0.29
BDC 10	4%	14%	0.055 ± 0.005	1.56 ± 0.18	2.46 ± 0.24	2.49 ± 0.24	0.22 ± 0.03	0.30 ± 0.05	4.62 ± 0.31

230

231

232 The external beta and alpha dose rates of the feldspar grains have been deduced from the
 233 radioisotopic contents of each sample, applying the conversion factors of Guérin et al. (2011), the
 234 attenuation factors of Guérin et al. (2012) for beta dose rate, or of Brennan et al. (1991) for alpha dose
 235 rate, and the alpha sensitivity correction (a-value of 0.086 ± 0.013) of Ree-Jones (1995). The
 236 radioisotopic contents of each sample were determined with high resolution gamma spectrometry
 237 (Canberra U-shaped germanium detector at low temperature).

238 U, Th and K activities or contents are reported in Table 3. No significant systematic disequilibrium can
 239 be detected in the U series. The activities of the coarse fractions are in most cases, except for BDC6,
 240 either consistent or up to $73 \pm 5\%$ higher (in particular for BDC2 and 8) than the ones for the fine
 241 fractions. In order to take into account auto-absorption and shielding phenomena induced by coarser
 242 materials of different radioisotopic contents, the beta dose rate was calculated on the one hand from
 243 the fine fraction, and on the other hand from the total (<1 cm) sample (Martin et al., 2015; Tribolo et
 244 al., 2017). This rate was calculated from the two activities' estimates (fine and coarse) and from the
 245 relative weight of the two fractions. The "fine" and "total" beta dose rates (beta 1 and beta 2,
 246 respectively, in Table 2) bracket the true mean beta dose rate and their mean is taken as the final
 247 estimate. For the alpha dose rate, only the activities from the fine fraction are taken into account.

248

249 *Table 3. ²³⁸U chain and ²³²Th chain activities or K contents estimated from different fractions of the samples. The total (<1cm)*
 250 *activities and contents are calculated from the measured activities and contents for the fine (<2 mm) and coarse (2 mm - 1*
 251 *cm) fractions and from the proportion of coarse material indicated in the third column of Table 2.*

252

253

254

255

	sample BDC	activities (Bq/kg)							content (%)		
		²³⁸ U series						²³² Th series	K		
		top		middle		bottom					
fraction <2 mm	1	37.7	± 2.7	25.6	± 0.4	32.7	± 5.1	50.1	± 0.6	2.47	± 0.04
	2	18.1	± 2.1	17.4	± 0.4	21.3	± 4.3	28.9	± 0.4	1.74	± 0.03
	3	31.3	± 3.0	27.8	± 0.5	24.0	± 5.8	45.8	± 0.6	2.19	± 0.04
	4	27.4	± 2.9	22.6	± 0.5	21.3	± 5.8	43.2	± 0.6	2.17	± 0.04
	5	23.9	± 2.5	21.4	± 0.4	23.7	± 4.9	34.5	± 0.5	1.81	± 0.03
	6	20.8	± 2.6	18.6	± 0.5	16.1	± 5.5	28.7	± 0.5	1.29	± 0.03
	7	21.8	± 2.5	21.6	± 0.5	25.2	± 5.1	35.9	± 0.5	2.18	± 0.04
	8	19.3	± 3.1	18.8	± 0.6	19.8	± 6.5	31.5	± 0.6	1.73	± 0.04
	9	29.2	± 3.1	27.4	± 0.5	18.8	± 5.8	50.2	± 0.7	2.71	± 0.05
	10	32.7	± 2.6	24.5	± 0.4	23.3	± 4.9	50.0	± 0.6	2.55	± 0.04
fraction [2mm - 1cm]	1	27.1	± 2.7	24.3	± 0.5	33.5	± 5.8	34.0	± 0.5	2.47	± 0.04
	2	29.1	± 2.8	30.1	± 0.5	27.9	± 5.7	37.1	± 0.6	2.40	± 0.04
	3	31.4	± 3.2	30.4	± 0.6	25.4	± 6.3	41.2	± 0.7	2.38	± 0.04
	4	31.7	± 1.9	29.5	± 0.4	21.1	± 4.1	42.9	± 0.5	3.00	± 0.04
	5	28.8	± 2.6	25.7	± 0.5	30.1	± 5.6	34.3	± 0.5	2.54	± 0.04
	6	13.2	± 1.9	13.7	± 0.3	9.5	± 3.9	22.6	± 0.4	1.09	± 0.02
	7	23.3	± 2.7	34.5	± 0.6	24.0	± 5.6	35.5	± 0.6	2.26	± 0.04
	8	31.2	± 3.4	29.7	± 0.6	28.5	± 6.9	42.5	± 0.7	3.15	± 0.06
	9	35.0	± 2.6	28.7	± 0.5	19.6	± 5.0	42.4	± 0.6	3.05	± 0.05
	10	32.7	± 2.9	29.6	± 0.5	25.8	± 5.7	39.1	± 0.6	2.89	± 0.05
total (< 1 cm)	1	36.0	± 2.7	25.4	± 0.4	32.8	± 5.1	47.5	± 0.6	2.47	± 0.04
	2	20.5	± 2.1	20.2	± 0.4	22.8	± 4.3	30.7	± 0.4	1.88	± 0.03
	3	31.3	± 3.0	28.0	± 0.5	24.1	± 5.8	45.4	± 0.6	2.21	± 0.04
	4	27.9	± 2.9	23.5	± 0.5	21.3	± 5.8	43.2	± 0.6	2.28	± 0.04
	5	24.4	± 2.5	21.8	± 0.4	24.3	± 4.9	34.5	± 0.5	1.88	± 0.03
	6	19.7	± 2.6	17.9	± 0.5	15.2	± 5.5	27.9	± 0.5	1.26	± 0.03
	7	22.1	± 2.5	23.7	± 0.5	25.0	± 5.1	35.8	± 0.5	2.19	± 0.04
	8	20.8	± 3.1	20.1	± 0.6	20.9	± 6.5	32.8	± 0.6	1.90	± 0.04
	9	30.6	± 3.1	27.7	± 0.5	19.0	± 5.8	48.2	± 0.7	2.79	± 0.05
	10	32.7	± 2.6	25.2	± 0.4	23.7	± 4.9	48.5	± 0.6	2.60	± 0.04

256

257

258

259 The gamma, alpha and beta dose rates must be corrected for moisture content, since water
260 absorbs a part of the radiative energy. The moisture content of each sediment sample at the time of
261 sampling was measured. It stands between four and seven percent (Table 2). We suggest that the
262 moisture content in the past was likely not much higher, given that evidence of fluid presence is limited
263 to localized minor precipitate formations, sporadic and locally constrained fluid run-off that did not
264 lead to substrate saturation, and the preservation of desiccated organic remains (see Sievers et al.,
265 2022 and Stratford et al., 2022). Therefore, the current water content was assumed to be
266 representative of past mean content. The gamma dose rate from the dosimeters was then taken as
267 such (since the *in situ* dosimeter already takes into account the impact of moisture during its burial).
268 For alpha and beta dose rates, correction factors of Zimmerman (1971) were applied. For the 63-80
269 μm feldspar grains, the final beta dose rates stand between 1.30 ± 0.12 and 2.48 ± 0.24 Gy/ka, and the
270 alpha dose rates between 0.13 ± 0.02 and 0.22 ± 0.03 Gy/ka.

271 For the potassium feldspar grains, an internal dose rate must also be taken into account. A mean
272 content of 12.5 ± 2.5 % K was applied following Huntley and Baril (1997) and supplemented with 400

273 ± 100 ppm Rb (Huntley and Hancock, 2001), resulting in an internal dose rate of 0.30 ± 0.05 Gy/ka. The
274 internal dose rate contributes from six to ten percent of the total dose rate.

275 The total dose rates for the feldspar grains stand between 2.89 ± 0.15 and 4.78 ± 0.29 Gy/ka, which is
276 higher than in most South African MSA sites.

277

278 6. Equivalent doses

279

280 Considering the high dose rates and the expected ages (>40 ka after the ESR and radiocarbon
281 results), most of the expected equivalent doses (D_e) are over 150 Gy for the quartz grains, and over
282 180 Gy for the feldspar grains. This suggests that the D_e s for quartz are likely close to saturation, thus
283 making their determination challenging.

284

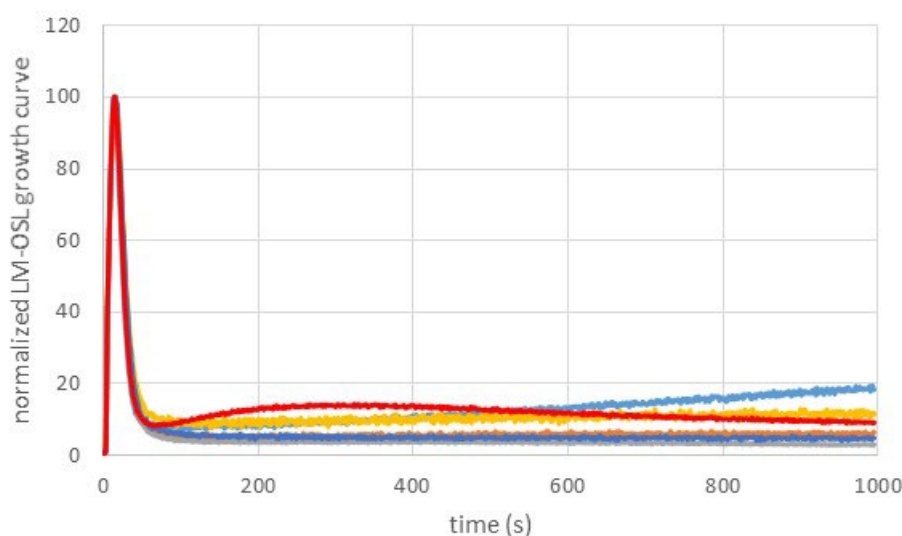
285 6.1 Quartz grains

286

287 A quartz OSL signal is known to be composed of several components, called fast, middle and
288 slow, depending on their bleachability. The fast component is the most suitable for standard protocols,
289 such as the single aliquot and regenerative dose protocol (SAR, Murray and Wintle, 2000). A LM-OSL
290 (linearly modulated OSL) test was conducted on the 40-63 μm quartz fraction (multi-grain cup) in order
291 to observe the signal components: the sequence, including a first LM-OSL measurement (blue LED at
292 125°C with power linearly increased from 0 to $100 \text{ mW}/\text{cm}^2$ in 1000 s), and cycles of dosing (100 Gy),
293 preheating and LM-OSL measurement was repeated by varying the preheating condition (none, 200°C
294 cut, 220°C 10 s, 260°C 10 s). The same protocol was applied to the Risø calibration quartz, known to
295 be dominated by the fast component (Hansen et al., 2015). We will not comment here on the effect of
296 the different preheating conditions. What must be emphasized is that the Border Cave quartz grains
297 are dominated by the fast component (Fig. 2).

298

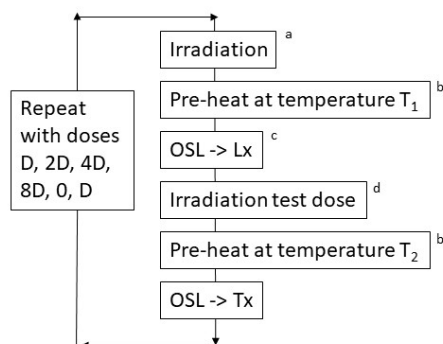
299



300

301 *Figure 2 : Normalized LM-OSL glow curves for different BDC samples, after a regenerative dose of 122 Gy and a cut-heat of*
302 *200°C. The red curve corresponds to the Risø calibration quartz (batch 123).*

303 To start with, the SAR protocol was tested on sample BDC3. A dose recovery test (DRT) was
 304 performed in order to check whether a known laboratory given dose would be accurately determined:
 305 the sample was bleached for one minute in a solar simulator (Hönle UVACube 400), left in the dark for
 306 over three hours and bleached again at room temperature with blue LEDs in the reader. Then, a known
 307 beta dose of 220 Gy was given in the reader and the SAR protocol (Fig. 3) was applied. An additional
 308 recycling cycle including an IRSL stimulation at 50°C was performed in order to check for feldspar
 309 contamination (Duller, 2003). The data have been analyzed with Analyst v4.57 (Duller, 2015). The
 310 growth curves were fitted with single saturated exponentials such as $L_x/T_x = a (1 - \exp(-(D+b)/D_0))$,
 311 where a , b and D_0 are the fitting parameters, L_x/T_x is the sensitivity corrected luminescence signal and
 312 D is the dose. Grains were rejected if their sensitivity was low (signal <3 times background; relative test
 313 dose error >10%), if the recuperation was high (ratio of signals for a 0 Gy dose and the highest
 314 regenerative dose >5%), and if the recycling was poor (recycling ratio not consistent with [0.9;1.1]).
 315 Grains were also rejected if their natural signal was higher than, or at, the saturation level. Since those
 316 grains are numerous (20% of the grains that pass the sensitivity and recuperation criteria for the DRT),
 317 an additional criterion based on the D_0 value was applied (Thomsen et al., 2016). It has been shown
 318 (see also Li et al., 2017) that when the true mean D_e is high, such that many grains are rejected because
 319 of saturation - i.e. because of low D_0 values - the estimated mean D_e of the remaining grains is
 320 underestimated. Following Thomsen et al. (2016) who suggest plotting D_e as a function of D_0 , one can
 321 generally observe the increase of the selected D_e values as a function of the D_0 values until a plateau
 322 is reached. This plateau occurs for the D_0 range values where no more grains are rejected because of
 323 saturation.

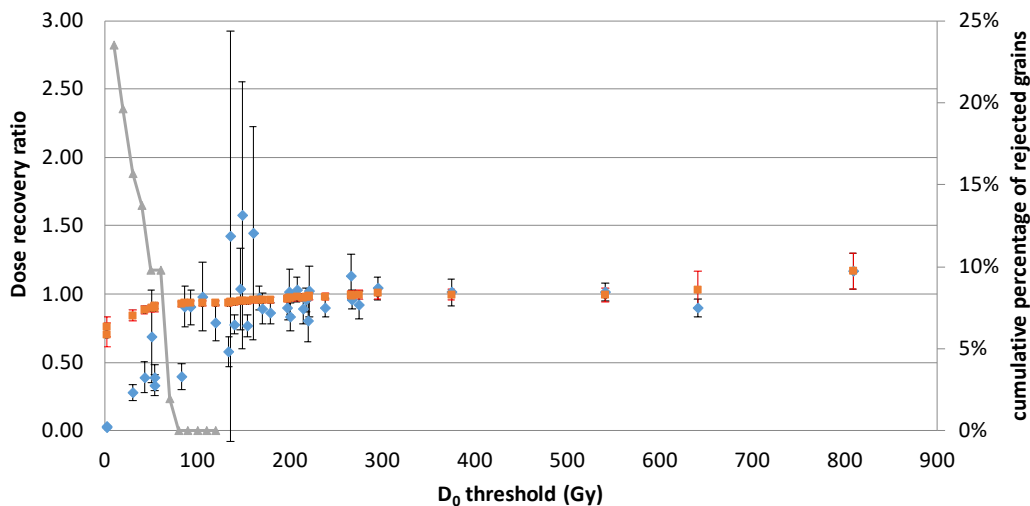


324

325 *Figure 3. SAR protocol. a) No irradiation was given during the first cycle, where the natural signal is measured. b) T_1 was fixed*
 326 *at 260°C for 10 s; T_2 was 220°C for 10 s; c) The signal is stimulated for 0.8 s. The first 0.05 s and last 0.1 s were taken as signal*
 327 *and back-ground respectively. d) Test dose was 37 Gy.*

328

329 Figure 4 displays the D_e/D_0 plot for sample BDC3. This sample has D_0 values well over 200 Gy, up to
 330 800 Gy, which is unusual for quartz grains. The 200-800 Gy range for the D_0 value is suitable for
 331 recording D_e s in the expected D_e range of the BDC samples. Moreover, in the plateau zone, the ratio
 332 of the central D_e (central age model, CAM, Galbraith et al., 1999) to the expected dose is consistent
 333 with unity at two sigma. This suggests *a priori* that the SAR protocol can be applied successfully at least
 334 for this sample, leading to an equivalent dose of 220 Gy. Interestingly enough, it is evident (Fig. sup.3)
 335 that the high D_0 grains are not the brightest grains, and inversely the brighter grains do not display D_0
 336 values >300 Gy. While bright grains are typically preferred (e.g. Anechitei-Deacu et al., 2018; Thomsen
 337 et al., 2012) we chose to investigate the dimmer – high D_0 grains further.



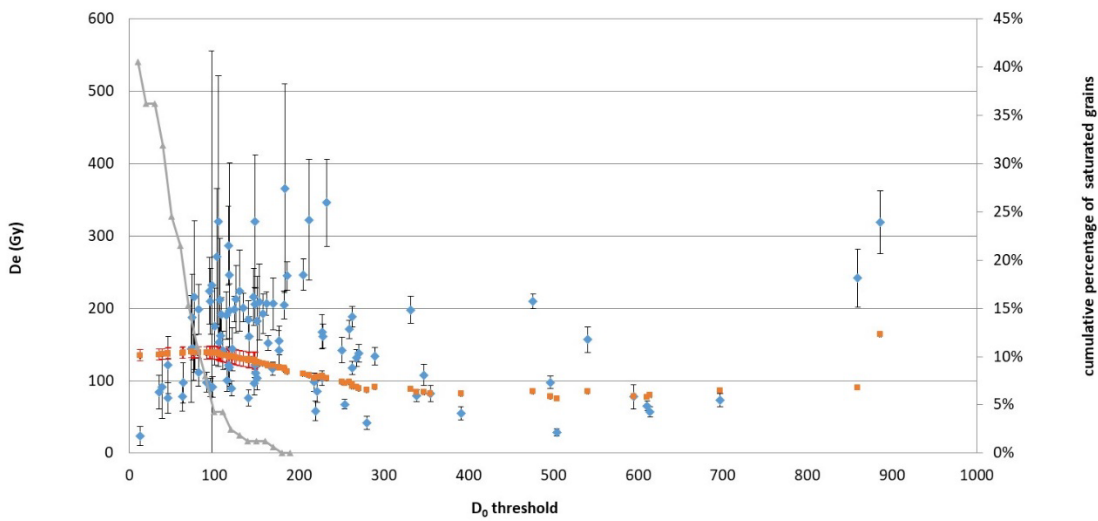
338

339 *Figure 4. D_e/D_0 plot for the dose recovery test of BDC3. The dose to recover was about 220 Gy. The blue dots represent the*
 340 *data for the grains that pass the rejection criteria. The orange dots correspond to the central dose (ratio) when only the grains*
 341 *above the corresponding D_0 threshold value are taken into account. The grey curve shows the cumulative percentage of grains*
 342 *that have been rejected because of saturation.*

343 The same protocol was then applied to the natural sample (BDC3). Figure 5 shows that in
 344 contrast to the dose recovery test, no clear plateau is reached for the highest D_0 values. On the
 345 contrary, unexpectedly low D_e values are obtained (mean <100 Gy), while the expected D_e is over 170
 346 Gy. Note that the D_0 /sensitivity pattern, however, remains identical (Fig. sup.4). This behavior was
 347 observed with other BDC samples as well (data not shown), and the reason for the dose drop was
 348 investigated.

349 In 2000, Yoshida et al. suggested using “supergrains”, i.e. grains with high D_0 values (and in their
 350 case, bright signals), in order to extend the age range of optical dating. On the other hand, many
 351 underestimates of high D_e s have been reported in the literature for quartz grains (Peng et al., 2022
 352 and references therein). This underestimate can be due to the presence of low D_0 values, and proper
 353 handling of single grain data has been shown in some cases to overcome this issue (Thomsen et al.,
 354 2016; Li et al., 2017). However, additional issues have been raised, such as, first, the domination by
 355 medium and/or slow components which are thermally unstable (e.g. Jain et al., 2003), fading in quartz
 356 of volcanic origin, or in some loess (Bonde et al., 2001; Tsukamoto et al., 2007; Perić et al., 2021), and,
 357 secondly, differences in competition for free charges, which can occur during stimulation and/or
 358 dosing and/or heating, between the traps and luminescence centers for natural and artificial dose rates
 359 (Bailey et al., 2004a). The consequence of this difference in competition is that the regenerative dose
 360 response curve is not equivalent to the natural dose response curve, and/or the natural test dose signal
 361 is not a good surrogate for the sensitivity of the natural signal (e.g. Singhvi et al., 2011).

362 Therefore, three hypotheses have been formulated: 1) is this quartz signal unstable? 2) Is there
 363 an issue of uncorrected sensitivity change? 3) Is there an issue with the scale of dose rate for natural
 364 versus artificial irradiation?



365

366 *Figure 5. De/D_0 plot for the De measurements of BDC3. The blue dots represent the data for the grains that pass the rejection*
 367 *criteria. The orange dots correspond to the central dose (ratio) when only the grains above the corresponding D_0 threshold*
 368 *value are taken into account. The grey curve shows the cumulative percentage of grains that have been rejected because of*
 369 *saturation.*

370

371

372 Hypothesis 1

373 While thermal instability has been reported for medium and some slow components (e.g. Jain
 374 et al., 2003), it is generally not expected for the fast component. To our knowledge, only Steffen et al.
 375 (2009) identified fast component instability for one of their samples, while being critical about their
 376 calculation of the trap lifetime. Since the BDC samples are dominated by the fast component, this
 377 instability is unexpected. However, the LM-OSL tests have been performed at the multigrain scale and
 378 the LM-OSL signal is dominated by the brighter grains which are not the high D_0 ones. Consequently,
 379 additional inspection of the glow curves was performed at the single grain level. Comparisons were
 380 made for CW-OSL glow curves of BDC3 (i.e. glow curves obtained with constant temperature and
 381 stimulation power) between those corresponding to D_0 values >300 Gy and those with D_0 values in the
 382 $[100-200$ Gy] interval displaying $De_s >180$ Gy (Fig. sup.5). No fast ratio such as the one defined by
 383 Durcan and Duller (2011) was calculated. Indeed, it requires the knowledge of the stimulation light
 384 intensity and photo-ionization cross-section of fast and medium component, which are not known in
 385 our measurement conditions and which appear to be variable with single grain stimulation (Duller,
 386 2012). Nonetheless, it is still possible to define an arbitrary ratio comparing the signal at the first
 387 channel (first 0.017s) and a later part of the signal (here 0.12-0.15 s) that allows for a partial description
 388 of the decay rate and comparison between the two groups. No correlation could be observed between
 389 the decay rates of the glow curve and the De values. In other words, the decay rates in the >300 Gy D_0
 390 /low De_s group is not slower than in the lower D_0 /higher De_s group (Fig. sup.6). We conclude that
 391 medium or slow components are not responsible for the drop of De_s with large D_0 values.

392 Fading issues (i.e. instability unpredicted by thermodynamics laws) are known to affect feldspar
 393 grains (see Section 6.2) and may lead to severe De underestimates if not corrected for. However, SEM-
 394 EDS analyses did not detect feldspar inclusions within the quartz grains, and IRSL tests (Duller, 2003)

395 did not suggest that the high D_0 / low D_e grains actually correspond to feldspar contaminants. Fading
396 has already been reported for quartz of volcanic origin (Bonde et al., 2001; Tsukamoto et al., 2007) or
397 from loess (e.g. Perić et al., 2021). Consequently, the fading rates for some of our quartz grains were
398 measured. Grains of a disc of sample BDC1 that showed a similar behavior to those of BDC3, were used
399 after the SAR measurements and identification of high D_0 grains. Successive cycles including irradiation
400 (180 Gy), preheat (260 °C 10 s), pause (delay of 0, 1, 10 and 100 hours), and single grain OSL
401 measurements (corrected for sensitivity change) were performed. The sensitivity-corrected signal was
402 then plotted as a function of the delay. The observation of the signal/delay relationship was hampered
403 by the high uncertainty of the signal and the high scatter of the data. Moreover, it was performed on
404 a limited number of grains. However, the mean fading rate of the high D_0 (here >200Gy) grains was
405 found to be consistent with 0, while one would expect for this sample a g value (at 2 days) of 12% in
406 order to explain the observed D_e underestimate in case of a logarithmic decay (Fig. sup.7). Therefore,
407 fading does not seem to be the cause of the low D_e values for the quartz grains.

408 *Hypothesis 2*

409 It is well known that the SAR protocol allows one to record and correct sensitivity changes that
410 occur from the first (natural) test dose measurement (Murray and Wintle, 2000), but that it cannot
411 guarantee that this first test dose is an appropriate surrogate of the sensitivity of the natural D_e signal.
412 Singhvi et al. (2011) have shown that sensitivity changes can occur during the measurement of the
413 natural OSL signal. They suggested using the 110°C TL peak measured before and after the natural
414 signal (using an additional small test dose) in order to correct for this issue, for multi-grain
415 measurements (Natural Sensitivity Corrected–SAR procedure). However, unless displaying one grain
416 per cup (Chauhan et al., 2019), which would be far too long to be practical, this is not applicable to
417 standard single grain measurements performed with single grain discs. Another possibility for
418 correcting early sensitivity changes, is to apply a single additive and regenerative dose protocol (SARA,
419 Mejdahl and Bøtter-Jensen, 1994). In this protocol, a known dose is added before the SAR protocol is
420 applied and the recovered dose is plotted as a function of the added dose (hereafter: SARA plot). In
421 cases where all sensitivity changes are properly taken into account (and do not depend on the added
422 dose), the slope of the plot is consistent with unity. However, if a sensitivity change occurs during the
423 natural signal measurement or between the natural (or natural+dose) and the subsequent test dose
424 measurement, the slope is different from unity and the correct D_e is deduced by extrapolation along
425 the X axis.

426 The SARA protocol was attempted on sample BDC6. Figure sup.8 displays the D_e/D_0 plots for
427 each added dose and Figure sup.9 shows the SARA plot obtained for D_0 values between 0 and 300, 300
428 and 600 and >600 Gy. The D_e/D_0 plots show that when a dose is added before the SAR measurements,
429 the D_e plateau appears at high D_0 values. Whatever the D_0 range, the slope of the SARA plot
430 significantly differs from unity, suggesting that there are indeed issues with sensitivity changes.
431 However, the corrected D_e drops from 332 ± 9 Gy for the 0-300 Gy D_0 range, to 103 ± 3 Gy for $D_0 > 600$
432 Gy. We conclude that the SARA protocol does not allow us to solve the issue of D_e underestimate for
433 the high D_0 values.

434 *Hypothesis 3*

435 Based on simulations, Bailey et al. (2004) suggested that the dose rate of the artificial source,
436 which is about 10^9 times higher than the natural dose rate, induces systematic overestimates of the
437 equivalent doses when they are >40 Gy. More recently, Peng et al. (2022), using a slightly different
438 quartz model, showed that the difference between artificial and natural dose rates could, on the
439 contrary, lead to systematic underestimates of the D_{e_s} . The over- or underestimates of the D_{e_s} are due

440 to significant differences in competition for free charges of the various traps and recombination
441 centers for low (natural) and high (artificial) dose rates. In order to mimic the natural state of
442 competition, Bailey et al. (2004) suggested applying pulse irradiations: the regenerative doses are split
443 under a series of smaller doses (typically 10 Gy) and a short preheat (240°C cut) is given after each
444 dose. This was attempted on sample BDC3 (Fig. sup.10). The main effect of this pulse irradiation mode
445 seems to be the disappearance of all D_0 values >400 Gy (with the standard irradiation mode, the high
446 D_0 values represent 11% of the non-saturated grains that pass the sensitivity and recuperation criteria),
447 and a clearer separation between grains that reach 200 Gy, and those that stay below 100 Gy.
448 However, it is not clear if this is only a statistical bias due to the low number of measured grains.
449 Meanwhile, the central D_e in the 150-400 Gy D_0 range (where no rejection for saturation occurs) is
450 even lower for the pulse irradiation group (101 ± 15 Gy) than for the standard irradiation group ($140 \pm$
451 11 Gy). This suggests that while the pulse irradiation may have an effect on the D_0 values, it does not
452 solve the issue of different competition levels, as initially suggested.

453

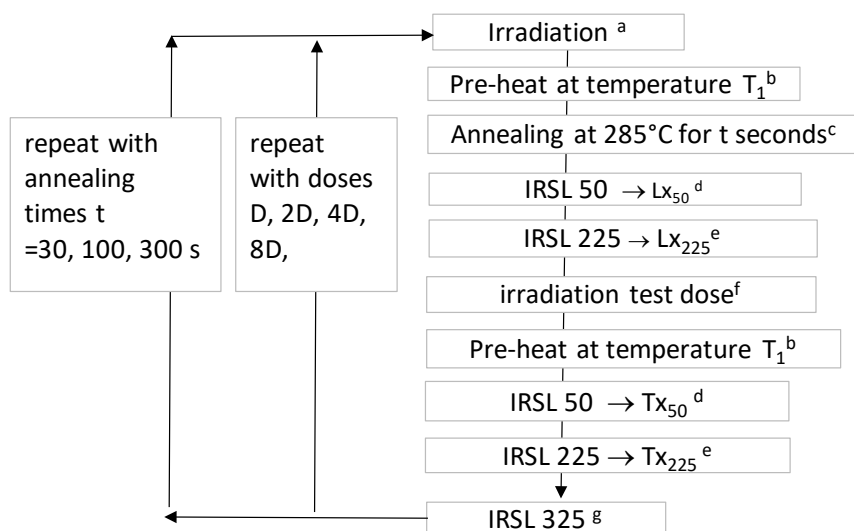
454 In summary, despite preliminary tests suggesting that quartz grains with high D_0 values could be
455 suitable for estimating the expected high D_e , only low D_{e_s} were obtained for those grains. While we
456 have tested two alternatives to overcome these issues (i.e. SARA protocol and pulse irradiations),
457 neither was found to be fully efficient. The new method recently proposed by Singhvi et al. (2021) to
458 adapt the multi-grain-natural correction factor to single grains could be considered in subsequent
459 work. Additional research should also explore whether the two groups of grains observed in the D_0
460 versus sensitivity plot are related to two different sources of grains, i.e. the aeolian part and the
461 weathering of the rhyolitic roof.

462

463 **6.2 Feldspars**

464

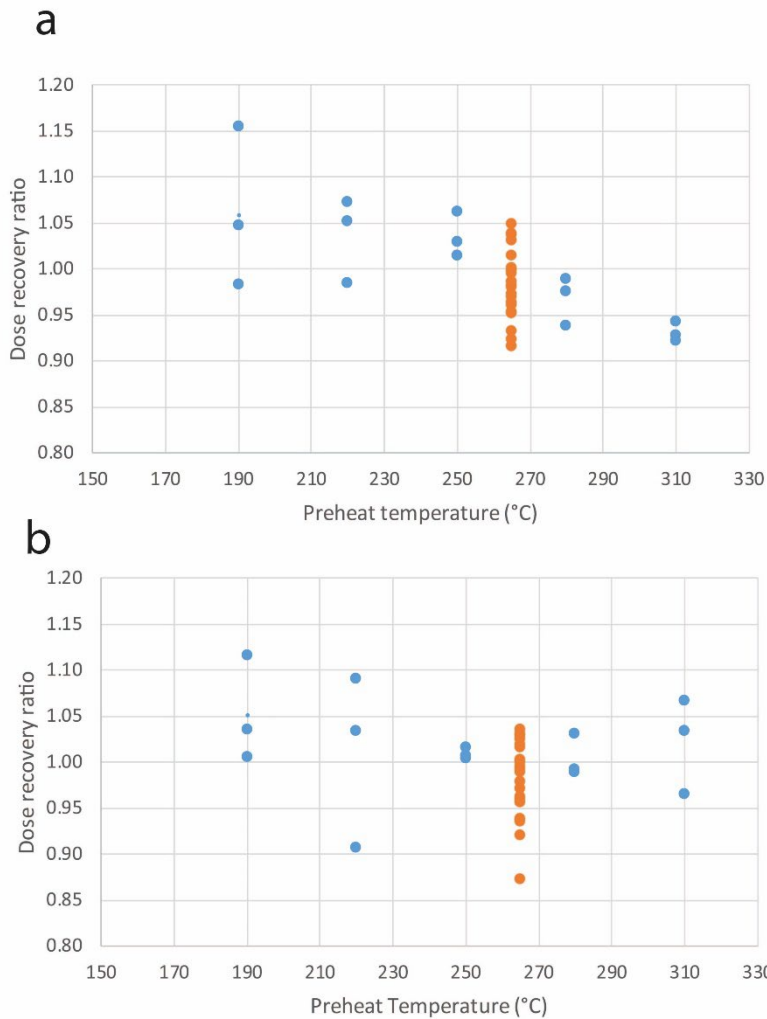
465 For the 63-80 μm feldspar grains, a post-isothermal post-IRSL (pIT) protocol (Lamothe et al.,
466 2020) has been applied (Fig. 6). This protocol, which uses both the IRSL signal at 50°C (IR50) and post-
467 IR50 IRSL signal at 225°C (IR225), allows one to take into account the fading rates of both signals
468 without the need to measure them. It is expected to give more accurate results than the standard IR50
469 or postIR50 IR225 or IR290 protocols. The pIT protocol is based on the observation that the decrease
470 of the growth curves due to fading can be mimicked in the laboratory by an annealing, i.e. an additional
471 thermal treatment performed between the regenerative dose and the standard preheat in a post-IR-
472 IRSL measurement cycle. In practice, growth curves are built for both the IR50 and IR225 signals for
473 different annealing times at a given temperature (the temperature has been shown not to be an
474 important factor). Ratios of the $D_{e_{\text{IR50}}}$ and $D_{e_{\text{IR225}}}$ obtained for these various annealing times are plotted
475 as a function of the $D_{e_{\text{IR50}}}$. This enables calculating the D_e for which this ratio is equal to unity: this one
476 corresponds to the fading corrected D_e (hereafter pIT D_e).



477

478 *Figure 6. pIT protocol. a) For the very first cycle, no irradiation is given since the natural signal is measured. b) For the first*
 479 *cycle and the first set of regenerative doses, no annealing is given. This corresponds to a standard post-IR50 IRSL225 protocol*
 480 *and is referred to later as annealing “0 s”. c) After the dose recovery tests, T_1 was fixed at 265°C for 60 s. d) The IRSL signal*
 481 *was stimulated for 200 s at 50°C. The first 6 s and last 20 s were taken as signal and background respectively. e) The IRSL*
 482 *signal was stimulated for 200 s at 225°C. The first 6 s and last 20 s were taken as signal and background respectively. f) The*
 483 *test dose was fixed at 139 Gy. g) An optical wash was performed with an IRSL stimulation at 325°C for 200 s in order to avoid*
 484 *signal recuperation. Note that all temperature increments were of 2°C/s in order to limit temperature overshoots and ensure*
 485 *better reproducibility of the measurements.*

486 First, the preheat temperatures have been adjusted in order to obtain dose recovery ratios
 487 consistent with unity: aliquots of sample BDC4 were bleached for about 1.25 hour in a solar simulator
 488 (Höhnle UVACube 400). Then they were given a dose of about 417 Gy and the post-IR50 IR225 protocol
 489 was applied (as in Figure 6, without any annealing time), using only one regenerative dose identical to
 490 the first dose, following Lamothe et al. (2018). The preheat temperature was increased from 190°C for
 491 60 s to 310°C for 60 s. The residual dose was estimated for a single preheat of 250°C for 60 s, but
 492 applied to correct all data. The dose recovery ratios for the IR50 and IR225 signals are shown in Figure
 493 7 (blue dots). The data suggest that a preheat temperature close to 270°C is most suitable. This was
 494 further tested on all samples with short dose recovery tests (only one regenerative dose, Figure 7,
 495 orange dots), and on some samples (BDC1, 3, 4, 5, 7, 9) with complete (five regenerative doses) dose
 496 recovery tests, with a preheat of 265°C for 10 s. The mean dose recovery ratio (Table sup.3) for both
 497 the IR50 and IR225 signals are within 5% of unity for the short DRT, and 10% of unity for the complete
 498 DRT. The 265°C preheat temperature was applied for the subsequent measurements.



499

500 *Figure 7. Dose recovery ratio as a function of the preheat temperature a) for the IR50 signal, b) for the IR225 signal. Only one*
 501 *regeneration of 417 Gy dose identical to the dose to recover was given for this test. Blue dots: BDC4, Orange dots: all other*
 502 *samples (3 dots/sample).*

503

504 Growth curves for an annealing temperature of 285°C and durations of 0, 30 and 100 s were
 505 built for 3 to 6 aliquots of each sample. The fit was done with an exponential plus linear saturating
 506 exponential. A few growth curves for an annealing time of 300 s were also built, but were found to be
 507 unnecessary in the post-processing of the pIT De calculation, so they will not be considered here. Since
 508 the measurement time for building one full set of growth curves for one aliquot and getting one pIT
 509 De is long (from 24 to 48 hours), it could be advantageous to apply a global growth curve (GGC)
 510 approach (e.g. Roberts and Duller, 2004; Li et al., 2015): a mean growth curve can be deduced from
 511 the full measurements of a first set of aliquots. Then, only the natural-sensitivity corrected signals
 512 (Ln/Tn) are measured on other aliquots and projected on the GGC.

513 The growth curves obtained on the different aliquots and samples have thus been compared in
 514 order to decide whether a GGC approach could be successfully applied or not. All Lx/Tx data have been
 515 gathered in figures 8a to 8f (one figure for each signal –IR50 or IR225-, and each annealing time, -0, 30,
 516 100 s-). The scatter increases with increasing annealing time and with increasing regenerative dose,
 517 but stands overall between 2 and 13% for all aliquots of all gathered samples. The GGC was then
 518 calculated for each annealing time and each IR signal. The pIT De based on the individual growth curves

519 and on the GGC have been compared (Table 4). Their ratio is within 10% of unity for aliquots of BDC1,
 520 3, 4, 5, 6, 9, but not for BDC2, 7, 8, 10. While BDC7 and BDC8, which are much older, are likely more
 521 sensitive to small changes in the growth curves, it is not the case for BDC2 and 10. On the other hand
 522 we do not have evidence that these samples have different mineralogical compositions, which would
 523 imply a different behavior. Consequently, the GGC approach has been applied to all samples. Only the
 524 global consistency of the results suggests *a posteriori* that this approach is relevant for all samples.

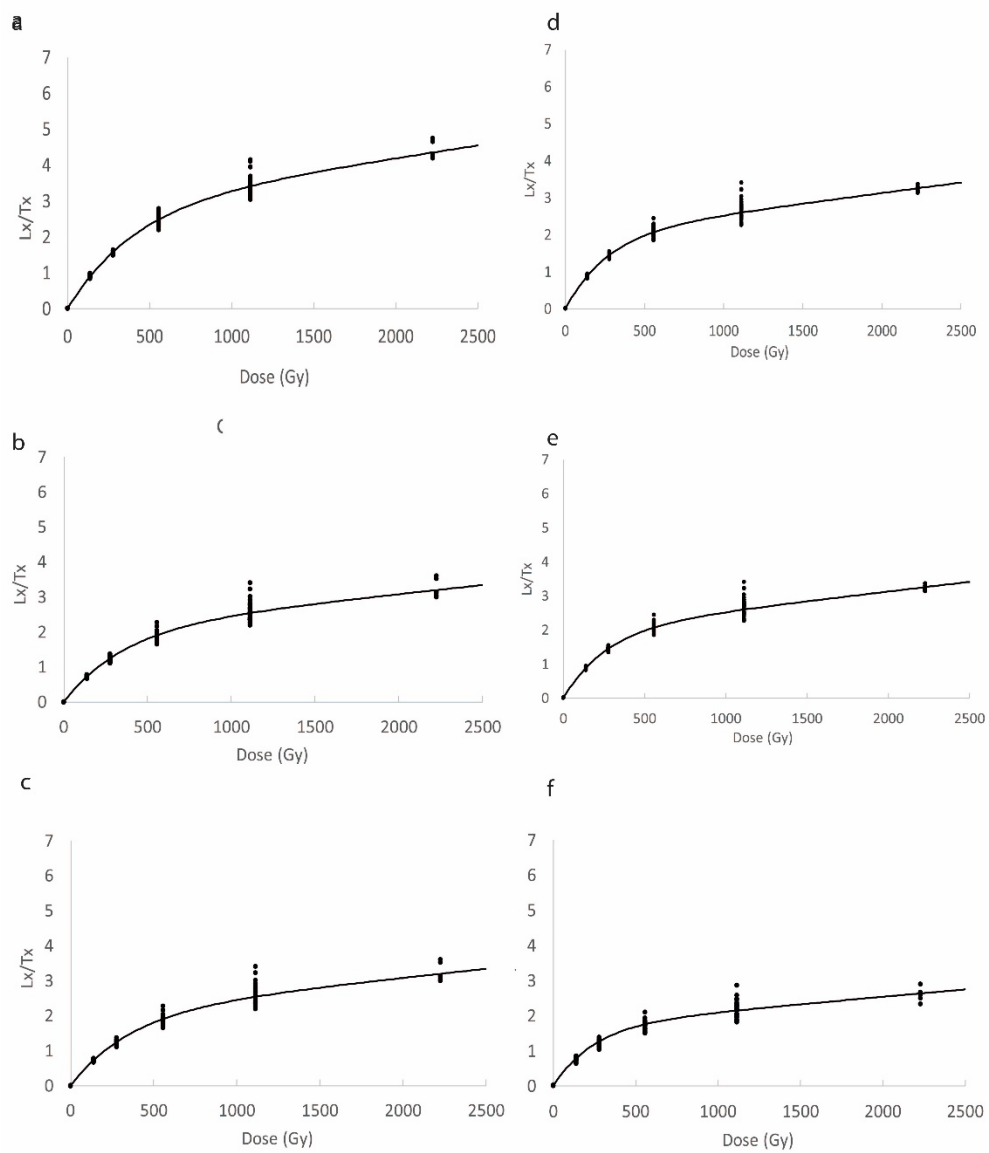
525 *Table 4. Comparison of De_s obtained with the individual growth curve approach (each aliquot is submitted to the full*
 526 *measurement protocol as shown in Figure 6), and with the GGC approach (the Ln/Tn values for each aliquot are projected on*
 527 *the mean growth curves calculated from all individual growth curves).*

BDC	global growth curves		individual growth curves		ratio GGC/individual De	
1	202	± 1	212	± 13	0.95	± 0.06
1	255	± 1				
1	216	± 1	227	± 2	0.95	± 0.01
2	276	± 2	376	± 4	0.73	± 0.01
2	253	± 2	295	± 3	0.86	± 0.01
2	260	± 1	277	± 1	0.94	± 0.01
2	239	± 1	273	± 4	0.88	± 0.01
3	266	± 1	269	± 9	0.99	± 0.03
3	344	± 2	375	± 10	0.92	± 0.02
3	257	± 1	269	± 2	0.96	± 0.01
4	311	± 2	324	± 2	0.96	± 0.01
4	389	± 2	356	± 4	1.09	± 0.01
4	301	± 1	320	± 2	0.94	± 0.01
5	407	± 3	398	± 6	1.02	± 0.02
5	366	± 2	367	± 4	1.00	± 0.01
5	335	± 2	316	± 2	1.06	± 0.01
6	304	± 2	321	± 2	0.95	± 0.01
6	345	± 2	334	± 1	1.03	± 0.01
6	310	± 2	308	± 1	1.01	± 0.01
7	1386	± 31	1458	± 20	0.95	± 0.02
7	1886	± 14	980	± 26	1.92	± 0.05
7	766	± 9	914	± 65	0.84	± 0.06
8	978	± 17	717	± 7	1.36	± 0.03
8	1250	± 28	1106	± 26	1.13	± 0.04
8	1655	± 24	889	± 10	1.86	± 0.03
9	418	± 6				
9	382	± 3	369	± 4	1.03	± 0.01
9	289	± 1	289	± 13	1.00	± 0.05
10	344	± 2				
10	230	± 1				
10	389	± 2	596	± 125	0.65	± 0.14
10	262	± 1	392	± 22	0.67	± 0.04
10	468	± 15	345	± 3	1.36	± 0.04
10	185	± 1	183	± 1	1.02	± 0.01

528
 529 Consequently, about 20 additional aliquots were measured for each sample in order to obtain Ln/Tn
 530 ratios. These were projected on the GGC and the corresponding De_{IR50} and De_{IR225} were calculated.
 531 Figure 9 displays three examples giving the ratio of the De_{IR50} and De_{IR225} as a function of De_{IR50} for each
 532 annealing time, which allows us to calculate the pIT De . In the inset of Figure 9, the ratio of the De_{IR50}
 533 and De_{IR225} is plotted as a function of the annealing time, allowing us to calculate the annealing time
 534 corresponding to the pIT De . Figure 10 displays the pIT De_s versus annealing times for each sample. For
 535 all samples in Figure 10, it can be observed that the pIT De_s slightly increase with the annealing times
 536 while they are expected to be independent. In order to understand this apparent correlation, we must
 537 observe the isodose plot (Fig. 11), where the mean Lx/Tx values for IR225 signals are plotted as a
 538 function of mean Lx/Tx values for IR50 signals for each annealing time and regenerative dose. The
 539 Ln/Tn values of each sample are also reported on this isodose plot. Lamothe et al. (2020, their Fig. 2)
 540 have indeed shown that each Lx/Tx (or Ln/Tn) couple corresponds to a single couple of pIT De and

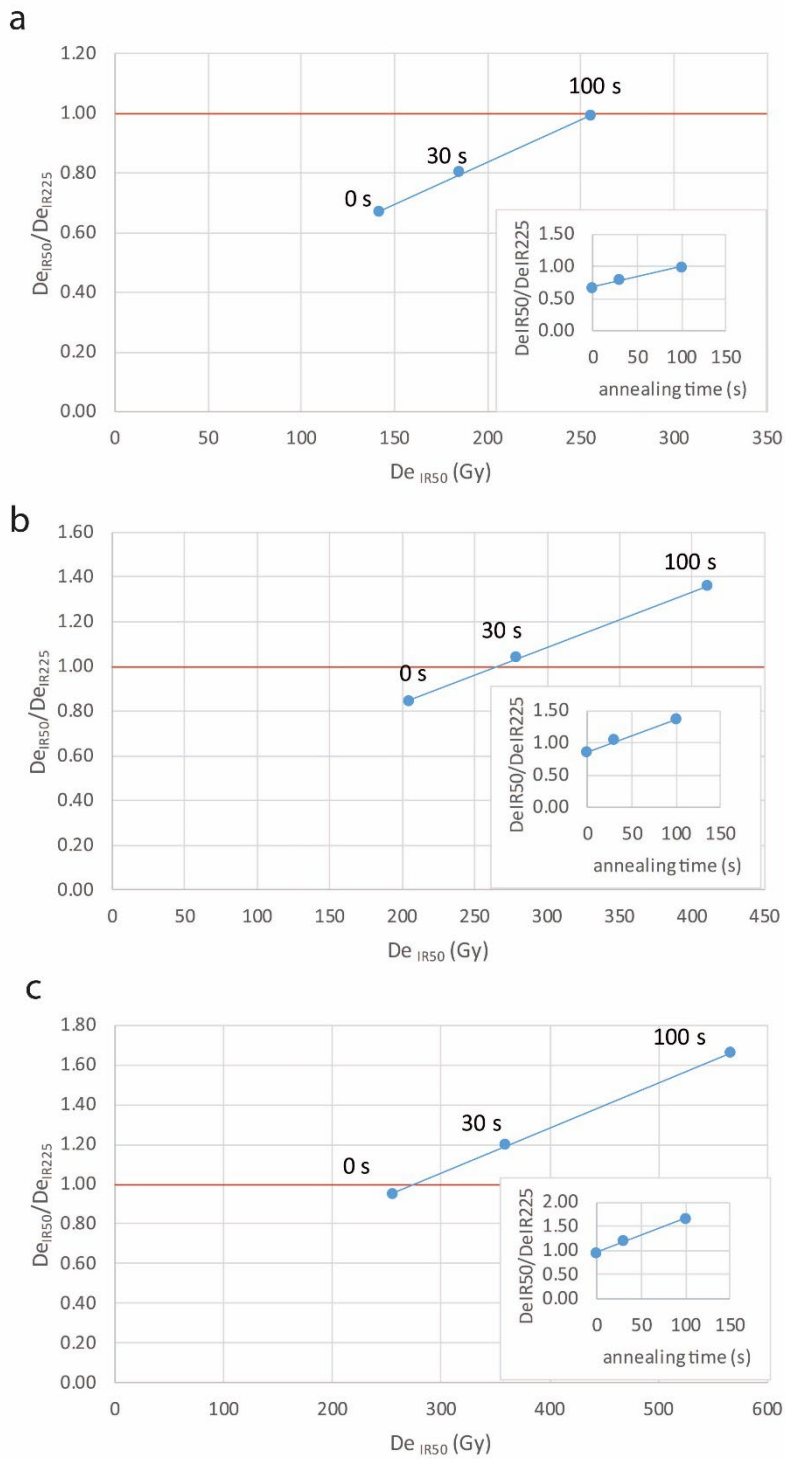
541 annealing time. Moreover, it can be deduced from this isodose plot that, if the IR225 signal had not
542 been properly bleached in the past, the position of the corresponding Ln/Tn point would be higher
543 than it should be. Consequently, it would appear as corresponding to a higher dose, with an apparent
544 higher annealing time. Considering our data plotted in Figure 11, we interpret the dependency of the
545 pIT De and annealing time as evidence for incomplete bleaching, at least for the IR225 signal which is
546 known to be less bleachable than the IR50 signal. This incomplete bleaching is unexpected if we
547 consider the aeolian component of the sediments and the slow sedimentation rates. However, part of
548 the grains also come from rhyolite fragments that fall off the roof and may have disintegrated while
549 already buried; hence, some grains might have not fully bleached.

550 Based on this interpretation, it can be concluded that the mean pIT De (Table 5) for each sample
551 likely overestimates the targeted De. Attempts have been made to apply the Minimum Age Model
552 (MAM, Galbraith et al., 1999), but results are extremely sensitive to the supposed over-dispersion of
553 the well bleached distribution, and we lack this information. On the other hand, if the lowest pIT De,
554 of each distribution correspond to well-bleached grains, then the extrapolated pIT De at 0 s annealing
555 should be consistent or lower than the targeted mean pIT De (Table 5). However, we cannot exclude
556 that none of the grains was actually fully bleached at time of deposition. Therefore, we will keep two
557 De estimates for each sample: the mean pIT De that we consider as a maximum De (it overestimates
558 the targeted De), and the 0 s annealing-extrapolated De estimate that we consider as a minimum De
559 estimate, in the case where some of the aliquots contain only grains that were fully bleached at
560 deposition. We expect the targeted age to be closer to (or consistent with) the minimum rather than
561 the maximum pIT age estimate.



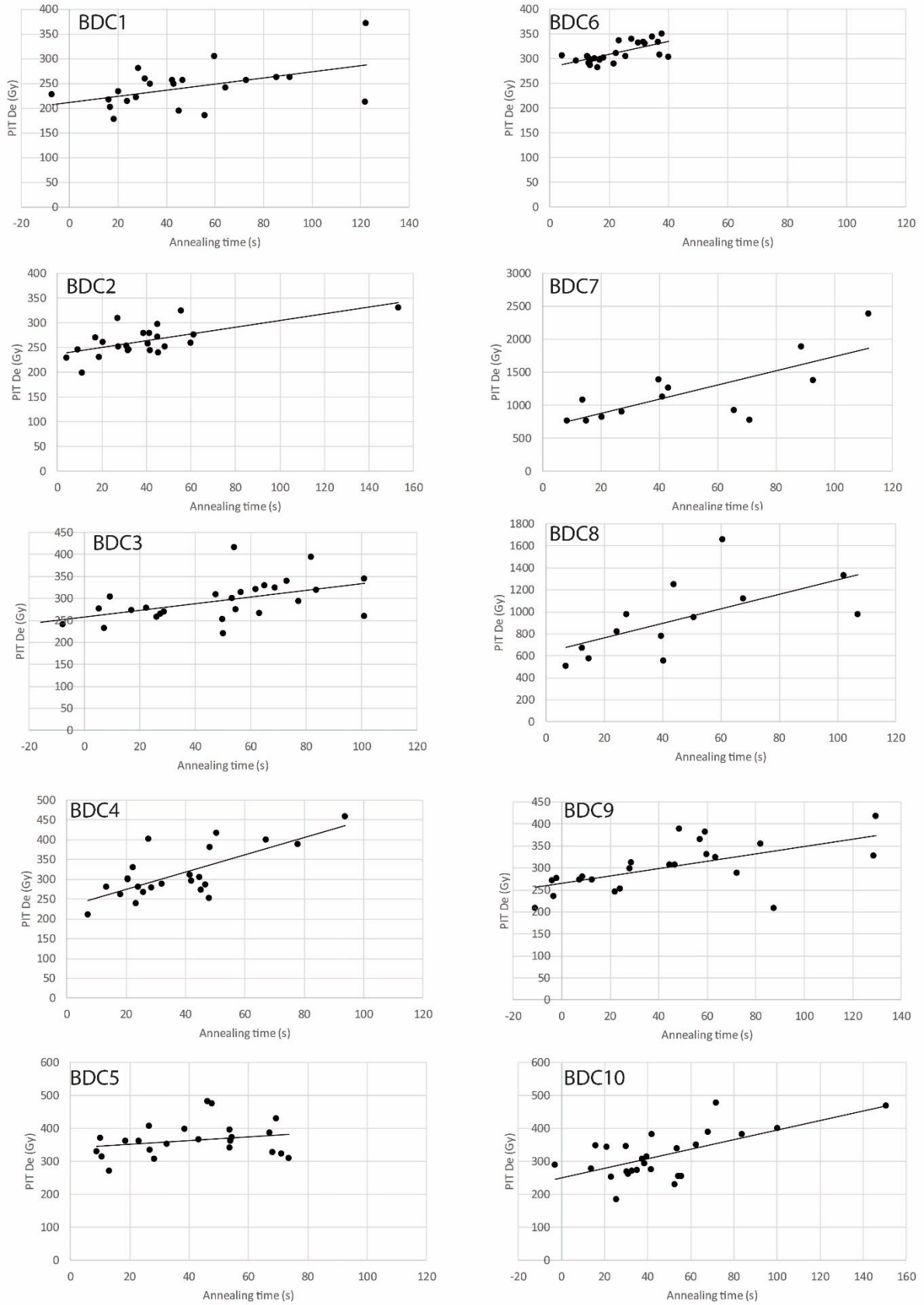
562

563 *Figure 8. Global growth curves calculated for all BDC samples (3 to 6 aliquots per samples). a: IR50, annealing 0 s; b: IR50*
 564 *annealing 10 s; c: IR50 annealing 30 s; d: IR225 annealing 0 s; e: IR225 annealing 30 s; f: IR225 annealing 100 s. The L_n/T_n*
 565 *signal of each aliquot can be projected onto each of these GGCs and the corresponding D_e is calculated by interpolation.*



566

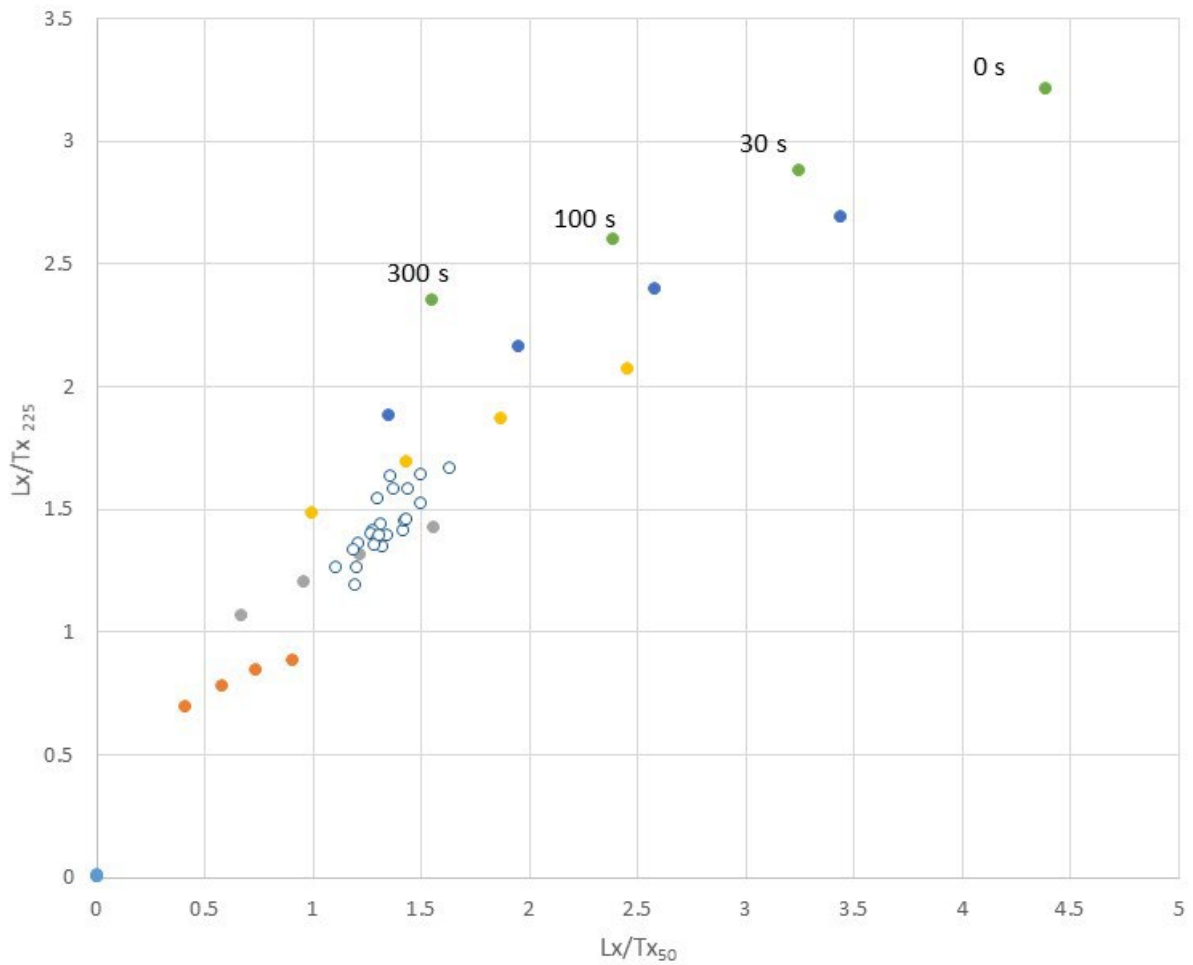
567 *Figure 9. Ratio of De_s for IR50 and IR225 signals for three different aliquots of BDC3 as a function of De_{IR50} (GGC approach).*
 568 *The interpolation allows one to calculate the fading corrected De (pIT De), i.e. the De for which the ratio is unity. In the inset*
 569 *the ratio is plotted as a function of the annealing times. The annealing time corresponding to a ratio equal to one can also be*
 570 *deduced by interpolation.*



571

572 *Figure 10. pIT De_s as a function of annealing times for each sediment sample. Linear regression curves highlight the fact that*
 573 *despite the scatter, in each sample the pIT De tends to increase with the annealing time. Error bars are smaller than the*
 574 *points.*

575



576

577 *Figure 11. Isodose plot. The mean Lx/Tx_{225} for each regenerative dose and annealing time of the GGC are plotted as a*
 578 *function of the mean Lx/Tx_{50} . The annealing times are indicated on the plot. Light blue dots: 0 Gy; orange dots: 139 Gy; grey*
 579 *dots: 278 Gy; yellow dots: 556 Gy; dark blue dots: 1113 Gy; green dots: 2227 Gy. White dots: Ln/Tn values for BDC4. This*
 580 *isodose plot constitutes a chart in a “fading corrected space”, where the $pIT De$ and corresponding annealing time for each*
 581 *Ln/Tn couple can be immediately deduced. However, in case of poor bleaching, Lx/Tx_{225} (and to a lesser extent Lx/Tx_{50}) will*
 582 *be higher than it should be. Consequently, the corresponding point will appear on a higher isodose curve and will correspond*
 583 *to an apparently higher annealing time. In other words, the poorer the bleaching, the higher the apparent $pIT De$ and the*
 584 *higher the apparent annealing time.*

585 Table 5. *pIT* De estimates for the 63-80 μm feldspar grains of the Border Cave samples. Two estimates are presented: the
 586 mean *pIT* De which overestimates the targeted De because of poor bleaching, considered as a maximum De estimate; the 0
 587 s-annealing extrapolated *pIT* De which underestimates or is close to the targeted De.

Sample	0 s annealing-extrapolated <i>pIT</i> De (Gy)		mean <i>pIT</i> De (Gy)	
BDC 1	212	± 15	241	± 9
BDC 2	236	± 9	264	± 6
BDC 3	257	± 16	295	± 9
BDC 4	231	± 20	313	± 13
BDC 5	341	± 23	364	± 11
BDC 6	282	± 8	312	± 4
BDC 7	660	± 169	1190	± 135
BDC 8	630	± 139	935	± 94
BDC 9	265	± 14	301	± 12
BDC 10	250	± 20	317	± 14

588

589

590 7. Ages and discussion

591 The minimum and maximum *pIT* ages are plotted in Figure 12 and given in Table 6. In Figure 12,
 592 we have also plotted the ESR age estimates (Grün et al., 2003), and the results of three different
 593 hierarchical Bayesian models. We will first discuss the Bayesian models, then compare the *pIT* ages
 594 with the Bayesian models, and finally discuss the archaeological and sedimentological implications.

595 As is commonly known, Bayes theorem allows one to combine chronological probabilistic
 596 information (e.g. radiometric or luminescence measurements) with probabilistic *a priori* information
 597 (e.g., stratigraphic ordering of archaeological and/or sedimentary levels) obtained from an
 598 archaeological site. When Bayesian age modeling methods are applied to an archaeological context,
 599 the age measurements (e.g., radiocarbon (^{14}C), OSL, ESR) and the *a priori* information lead to a
 600 *posteriori* results that improve our understanding of the timing and duration of archaeological events.

601 Bayesian models based on ^{14}C dates and *a priori* chronostratigraphic information have become
 602 very common during recent decades. In cases where ESR and OSL data are included in a Bayesian
 603 model, additional issues must be considered because such ages (when obtained for a given
 604 stratigraphic sequence) are not fully independent since they potentially share parameters (e.g. cosmic
 605 or gamma dose rate) and systematic uncertainties (Rhodes et al., 2003). Not taking this special feature
 606 into account can lead to an underestimation of the uncertainties associated with the *a posteriori*
 607 results. While specific methods have been developed (e.g. Philippe et al., 2019), Millard (2006) was the
 608 first to propose a relevant Bayesian method integrating a hierarchical approach adapted to ESR ages,
 609 which he applied to the Border Cave ESR data. His calculations were run on the ESR data available for
 610 each subsample (two or three per tooth), corrected for the cosmic dose rate (following Grün et al.,
 611 2003), using WinBUGS, and assuming continuous deposition without any hiatuses. The results for each
 612 tooth are presented only graphically in the 2006 paper, but the 95% Highest Posterior Density (HPD)
 613 for the boundaries have been kindly provided by A. Millard (pers. comm) and are reported in Table
 614 sup.4 and Figure 12.

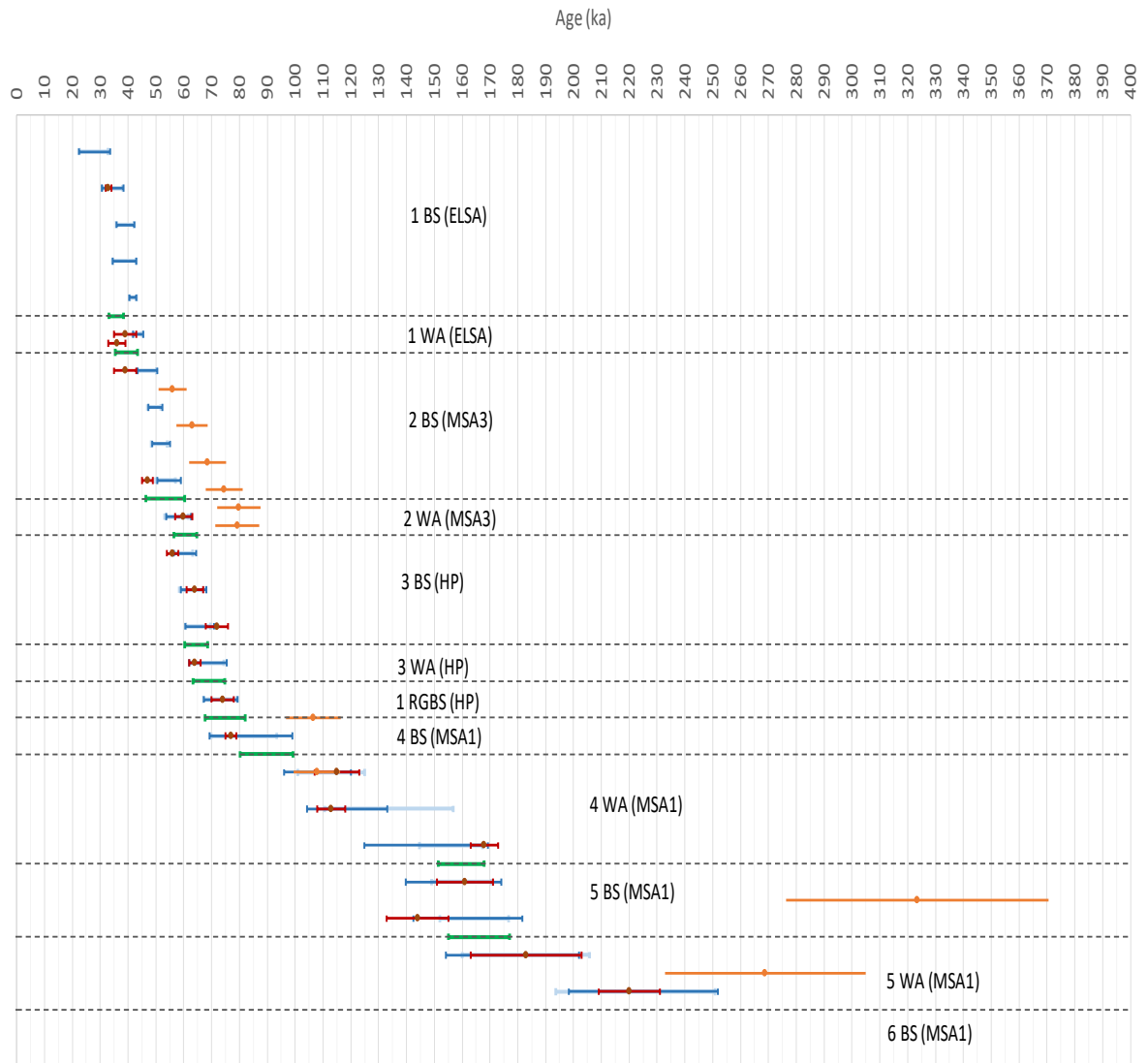
615 In addition to Millard's analyses, we produced two hierarchical Bayesian age models using the
 616 ChronoModel software package (Lanos and Dufresne, 2019; Lanos and Philippe, 2018), and the reasons
 617 for this choice are detailed in the Supplementary Information in Section 5. The advantage of
 618 ChronoModel is that the Event concept, on which it is based, avoids the compression effect that occurs

619 in packages that employ the Naylor-Smith-Buck-Christen (NSBC) prior (which is used in software
620 packages such as BCal or OxCal; Bronk-Ramsey, 2001; Buck et al., 1999; Lanos and Philippe, 2018). In
621 addition, ChronoModel's hierarchical model automatically penalizes outliers, so there is no need to
622 reject data before running the model or to run multiple generations of a model, for early generations
623 are used to identify outliers, which are removed before running a subsequent model. Our models
624 employed all available radiocarbon and ESR data (also corrected for the cosmic dose rate) and assumed
625 continuous deposition without any hiatuses. Two models were run: one in which each subsample is
626 taken into account, and all the subsamples of a tooth, together, constitute an Event; and a second one
627 in which an average ESR age for each tooth constitutes an Event.

628 The two models we produced with ChronoModel compare well with the one produced by
629 Millard (Table sup.5, Fig. 12), despite differing mathematical foundations. The small shift for the
630 boundaries of 1 WA/1 BS and 2 BS/1 WA is likely due to the fact that Millard did not incorporate the
631 then available ¹⁴C ages. This observation shows that, although Millard's model takes into account more
632 finely the dependence between samples and the systematic uncertainties they share, the results of
633 our Bayesian models are primarily governed by the *a priori* information, such as stratigraphic
634 relationships, since the Event date concept is the central element of our models.

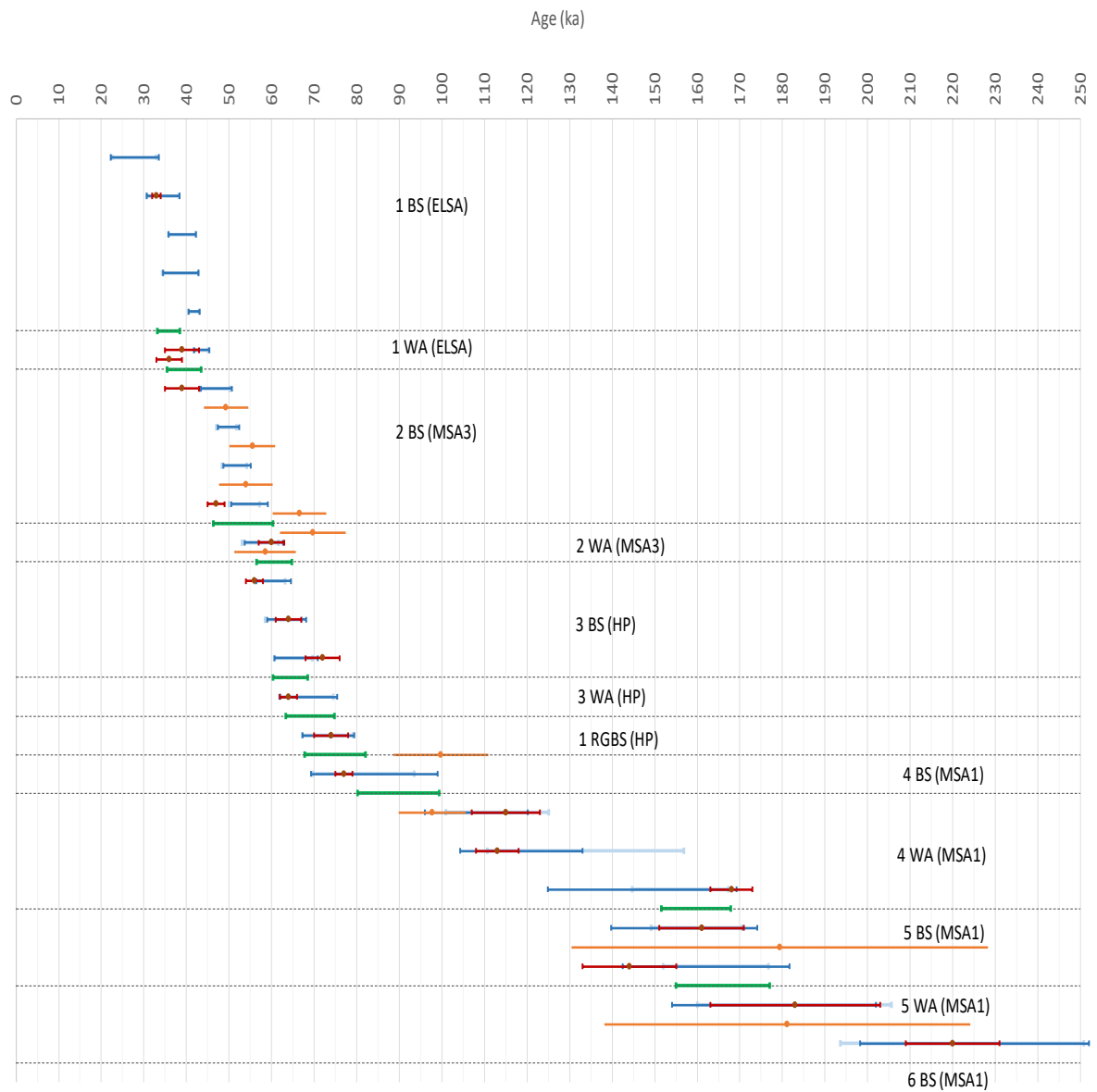
635

636



637

638



640

641

642 *Figure 12. Synthesis of ages for the Border Cave stratigraphic sequence. Red dots: ESR ages from Grün et al. (2003; mean for*
 643 *each layer). Dark blue and light blue bars: Bayesian models based on ESR and radiocarbon data. Dark blue: from ages for each*
 644 *tooth subsample; Light blue: from the average ESR ages for each tooth. Green bars: Bayesian models for transition between*
 645 *members based on the ESR ages, after Millard (2006). Orange dots: ages from feldspar grains obtained with the pIT protocol.*
 646 *Top figure: mean pIT age estimates. Bottom figure: minimum pIT age estimates. ESR and pIT ages are given at 1 σ , while*
 647 *Bayesian results present the 95% HPD.*

648

649

650

651

652 *Table 6. Ages based on the pIT protocol applied to 63-80 μm feldspar grains. The samples are ordered following the same*
 653 *stratigraphic order as in Figure 12. The relative stratigraphic correlations between BDC1 and 2 as well as BDC9 and 10 are*
 654 *speculative.*

sample	member	excavation area	layer	cultural attribution	minimum age (ka)		maximum age (ka)	
BDC 1	2 BS	northern	Grass Mat Camilla	MSA 3	49	± 5	56	± 5
BDC 9	2 BS	southern	Brown Caby	MSA 3	55	± 5	63	± 6
BDC 2	2 BS	northern	Yellowish Brown Caz	MSA 3	67	± 6	75	± 7
BDC 10	2 BS	southern	Brown Caby	MSA 3	54	± 6	69	± 7
BDC 3	2 WA lower	northern	Dossy unit above combustion feature 3	MSA 3	70	± 8	80	± 8
BDC 4	2 WA lower	northern	Dossy unit above combustion feature 3	MSA 3	58	± 7	79	± 8
BDC 5	1 RGBS/4 BS	northern	Very Dark Brown Faan	HP/MSA 1	100	± 11	106	± 10
BDC 6	4 WA	northern	White Idaho	MSA 1	98	± 8	108	± 8
BDC 7	5 BS	northern	Brown John	MSA 1	179	± 49	324	± 47
BDC 8	5 WA	northern	Dark Brown Kevin	MSA 1	181	± 43	269	± 36

655

656

657

658 In Figure 12, elevations relative to datum point for individual samples are not reported because
 659 such information is lacking for the ESR samples and also because of the slope of the deposits (deposits
 660 have a pronounced gradient and so single units have a wide range of elevations, i.e. an elevation
 661 cannot be correlated directly to a whole unit). Moreover, within a member, the relative stratigraphic
 662 relationship between the ESR samples from Peter Beaumont’s excavations and the pIT samples from
 663 the current excavation, cannot be determined with precision. Within a member, only the relative
 664 relationship between the ESR samples, on the one hand, and between the pIT samples, on the other,
 665 are meaningful. In addition, BDC1, 2 and BDC9, 10, are all attributed to 2 BS but come from different
 666 exposed excavation sections and it is not clear yet how the 2 BS subunits in the northern stratigraphy
 667 correlate with the southern 2 BS excavation. So, their relative stratigraphic positioning within each
 668 member in Figure 12 is not indicative of their relative intra-member stratigraphic relationship.

669 While the maximum pIT age estimates are significantly higher than the ESR age estimates and
 670 their Bayesian models, the minimum pIT age estimates are consistent with these ones, in particular for
 671 the top samples (the error estimates for BDC7 and 8 in Members 5 BS and 5 WA are unfortunately very
 672 large, so not very informative). Therefore, if our assumption that the targeted ages are close to the
 673 minimum pIT age estimates is correct, these results suggest both that the ESR-based chronology and
 674 its derived Bayesian models do not have to be challenged and that general attribution of the new
 675 excavation to the macro-scale stratigraphic framework of Beaumont is currently acceptable. Improving
 676 intra-member stratigraphic resolution will provide significant benefits in tracing changes that fall
 677 within error margins of dating methods, and be useful targets for future chronological research.

678 Border Cave has long been known to be one of the rare sites, along with Diepkloof Rock Shelter
 679 (Tribolo et al., 2013), where ages older than 65 ka have been obtained for the Howiesons Poort levels.
 680 Jacobs et al. (2008) have argued that the pattern observed at Border Cave was probably only a
 681 statistical issue (due to the large uncertainties) and that the ESR data from Border Cave were actually
 682 consistent at two sigma with their estimate of 65 ± 3 ka (95% CI) for the start of the Howiesons Poort
 683 (revised to 62-71 ka in Jacobs and Roberts, 2017). The new data do not invalidate the >65 ka ages for
 684 the members that have been attributed to the Howiesons Poort by Beaumont (e.g. Grün and
 685 Beaumont, 2001). Sample BDC5, in particular, at the base of the members attributed to the Howiesons
 686 Poort is too imprecise both spatially and temporally. Further sampling in 3 BS, 3 WA and 1 RGBS would
 687 be helpful for further clarification. However, most importantly, new technological analyses of the
 688 concerned members suggest that the Howiesons Poort cultural attribution as a whole needs to be
 689 taken with caution. In his Master’s thesis, Beaumont (1978) attributed 3 BS, 3 WA and 1 RGBS to “Epi-
 690 Pietersburg of the old-second intermediate”, renamed Howiesons Poort in Grün and Beaumont (1990).

691 This was based on the presence of blades, backed elements and '*Châtelperron or Abri Audi knives*' and
692 sometimes small, pressure-flaked arrowheads. We found very few of them in our new excavation (e.g.
693 only one *Châtelperron* backed piece in Member 1 RGS layer Ea and one backed piece in 1 RGS layer
694 Easy). However, in the upper Members 2 WA and 2 BS, Beaumont also mentioned trapeze backed
695 pieces, which he drew as some of the most characteristic items of the MSA 3/post-Howiesons Poort at
696 Border Cave. Hence, at Border Cave, as with other MSA sites in South Africa (e.g. Sibudu Cave) where
697 they also appear in pre-Still Bay, Still Bay, and post-Howiesons Poort layers, isolated backed pieces
698 cannot be used as an unequivocal marker for the Howiesons Poort.

699 The current chronological data do not necessarily clarify our understanding of hiatuses or
700 erosional phases observed in the stratigraphy (Stratford et al., 2022). For example, the current
701 temporal resolution is not sufficient to highlight several sedimentological sub-units with
702 disconformities that appear in Members 2 WA and 5 BS (Stratford et al., 2022), including a
703 technological change within Member 2 WA (de la Peña et al., in press). Layer Brown Caby, in Member
704 2 BS, dated with BDC9 and 10 has a low frequency of artefacts, but its age is indistinguishable from the
705 ages for the relatively artefact rich underlying Member 2 WA. A truncation is also observed between
706 Members 5 BS and 5 WA (Stratford et al., 2022) but it is not obvious in the chronological data. The
707 current uncertainties are too large to identify these sedimentological breaks, and/or the sampling was
708 not sufficient in scope to constrain them adequately. This limitation is not unique to Border Cave and
709 is common in many archaeological sequences. Increasing dating sampling frequency in response to
710 increased stratigraphic resolution, however, may not meaningfully provide additional chronological
711 resolution due to inherent uncertainties. Refinement of the age model will be possible when hiatuses
712 are identified and added to ChronoModel and when additional site formation and material culture
713 data are obtained.

714 On the other hand, apparent chronological gaps, which were already highlighted by Grün and
715 Beaumont (2001) warrant further investigation. This concerns in particular the transition between 4
716 BS and 4 WA with only one sample (BDC6) at 100 ka filling a gap between ca. 85 ka and 120 ka, the
717 middle of 4 WA with the lack of chronological data between approximately 120 and 150 ka (remarkably
718 4 WA represents the member covering the longest interval of time, nearly 70 ka, displaying numerous
719 sub-units), and the base of 5 WA, with the ESR age (and potentially pIT age, though again the
720 uncertainty is too large) at 174 ± 9 ka and the last one at 227 ± 11 ka. We need to clarify whether these
721 apparent gaps are due to a lack of sampling, a halt in sedimentation and archaeological record, or
722 erosion. The base of the sequence (Member 6 BS) should also be sampled for future dating in order to
723 document the deposition of geogenic and anthropogenic sediments in the empty shelter.

724 Meanwhile, the implications of the ages obtained in this study for our understanding of the
725 Middle Stone Age in southern Africa are significant, and some will only be appreciated with further
726 excavations at the site and at other sites in the region. Despite their consistency and good agreement
727 with the chronology of the upper layers established through numerous ^{14}C ages, the ages obtained in
728 the past for the lower layers of Border Cave have been viewed with some degree of caution due to the
729 implementation of a single dating method, a preliminary and shifting attribution of lithic industries to
730 the techno-complexes in favour at the time of excavation, and the lack of other regional reference
731 sequences covering a time span as extensive as that covered by this site. The ages obtained in our
732 study definitely anchor the archaeological layers of this long sequence in a chronological framework
733 that can be considered as established, even if not perfect. In the future, when the abundant lithic
734 industries present in the sequence (de la Peña et al., in press) have been characterized and coupled
735 with a refinement of the archaeological layers and their mode of formation (Stratford et al., 2022), our
736 present chronological framework will undoubtedly reverberate with other sequences in the region and
737 sub-continent.

738

739

740 **8. Conclusion**

741 Following the recent excavations at Border Cave (Backwell et al., this volume), we have re-
742 evaluated the site's chronology via the application of TL to burnt lithics, OSL to quartz grains and IRSL
743 (pIT protocol) to feldspar grains. Both TL and OSL failed for the samples that we tested. The current
744 pIT data, while perfectible, confirm the ESR chronology and validate the tentative identification and
745 attribution of the member boundaries recognized by Backwell and colleagues following Beaumont's
746 member framework. Additional sampling can be refined on that basis in order to explore hiatuses and
747 sedimentation rates. However, poor bleaching might still affect the results. Further methodological
748 improvements will: 1) attempt to work on smaller aliquots, up to single grain aliquots in order to try
749 to isolate fully bleached grains; and 2) correct for the poor bleaching via the new approach proposed
750 by Lamothe et al. (2021). Moreover, while we have measured only Ln and Tn signals, an additional
751 regenerative dose could be measured in order to apply the regeneration normalization method (re-
752 normalization, Li et al., 2015), which has the advantage of reducing the scatter between the growth
753 curves. These improvements, together with additional sampling, will help to further clarifying Border
754 Cave's chronology.

755

756

757

758

759 **Acknowledgements**

760 This research was funded by a National Geographic Explorer grant (NGS-54810R-19) and DSI-
761 NRF Centre of Excellence in Palaeosciences (Genus) grant (CEOOP2020-1) to Lucinda Backwell.
762 Francesco d'Errico's work is supported by the Research Council of Norway through its Centres of
763 Excellence funding scheme, SFF Centre for Early Sapiens Behaviour (SapienCE), project number
764 262618, the LaScArBx research programme (ANR-10-LABX-52), and the Talents Programme [grant
765 number: 191022_001]. Work by CT, NM, NB, FD, NC, WEB and FdE was supported by the Grand
766 Programme de Recherche 'Human Past' of the Initiative d'Excellence (IdEx) of Bordeaux University. We
767 are grateful to Amafa for issuing us with an excavation permit (SAH 15/7645). Special thanks to Michel
768 Lamothe for his help and advice concerning the pIT protocol. Thank you also to Andrew Millard for
769 providing the numerical values for the age boundaries of the various members.

770

771

772

773

774 **References**

775 Anechitei-Deacu, V., Timar-Gabor, A., Thomsen, K.J., Buylaert, J.P., Jain, M., Bailey, M., Murray, A.S.,
776 2018. Single and multi-grain OSL investigations in the high dose range using coarse quartz.
777 *Radiat. Meas.* 120, 124-130.

778 Backwell, L., Wadley, L., d'Errico, F., Banks, W.E., de la Peña, P., Sievers, C., Stratford, D., Lennox, S.,
779 Wojcieszak, M., Bordy, E., Bradfield, J., 2018. New excavations at Border Cave, KwaZulu-Natal,
780 South Africa. *J. Field Archaeol.* 43(6), 417-436.

781 Backwell, L., Wadley, L., d'Errico, F., Banks, W., de la Peña, P., Stratford, D., Sievers, C., Laue, G., Vilane,
782 B., Clark, J., Tribolo, C., Beaudet, A., Mauran, G., 2022. Border Cave: A 227,000-year-old archive
783 from the southern African interior. *Quaternary Sci. Rev.* 291: 107597.

784 Bailey, R.M., 2004. Paper I-simulation of dose absorption in quartz over geological timescales and its
785 implications for the precision and accuracy of optical dating. *Radiat. Meas.* 38(3), 299-310.

786 Beaumont, P. B., 1978. Border Cave. M.A. dissertation, University of Cape Town. South Africa.

787 Beaumont, P.B., 1980. On the age of Border cave hominids 1-5. *Palaeontol. Afr.* 23, 21-33.

788 Beaumont, P.B., de Villiers, H., Vogel, J.C., 1978. Modern man in sub-saharan Africa prior to 49000 BP:
789 a review and evaluation with particular reference to Border Cave. *S. Afr. J. Sci.* 74, 409-419.

790 Beaumont, P.B., Vogel, J.C., 1972. On a new radiocarbon chronology for Africa south of the Equator:
791 part 2. *Afr. Stud.* 31(3), 155-182.

792 Beaumont, P.B., Miller, G.H., Vogel, J.C., 1992. Contemplating old clues to the impact of the future
793 greenhouse climates in South Africa. *S. Afr. J. Sci.* 88, 490-498.

794 Bird, M.I., Fifield, L.K., Santos, G.M., Beaumont, P.B., Zhou, Y., Di Tada, M.L., Hausladen, P.A., 2003.
795 Radiocarbon dating from 40-60 ka BP at Border Cave, South Africa. *Quaternary Sci. Rev.* 22, 943-
796 947.

797 Bonde, A., Murray, A., Friedrich, W.L., 2001. Santorini: luminescence dating of a volcanic province using
798 quartz? *Quaternary Sci. Rev.* 20(5-9), 789-793.

799 Bøtter-Jensen, L., Bulur, E., Duller, G.A.T., Murray, A.S., 2000. Advances in luminescence instrument
800 systems. *Radiat. Meas.* 32, 523-528.

801 Brennan, B.J., Lyons, R.G., Phillips, S.W., 1991. Attenuation of alpha particle track dose for spherical
802 grains. *Nucl. Tracks Rad. Meas.* 18, 249-253.

803 Bronk Ramsey, C., 2001. Development of the radiocarbon calibration program OxCal. *Radiocarbon* 43,
804 355-363.

805 Buck, C., Christen, J., and James, G., 1999. BCal: an on-line Bayesian radiocarbon calibration tool.
806 *Internet Archaeol.* 7.

807 Chauhan, N., Singhvi, A.K., 2019. Changes in the optically stimulated luminescence (OSL) sensitivity of
808 single grains of quartz during the measurement of natural OSL: Implications for the reliability of
809 optical ages. *Quat. Geochronol.* 53, 101004.

810 Cooke, H.B.S. 1941. Unpublished reports presently housed at the National Archives and Records
811 Service (NARS) in Tswana (formerly Pretoria), South Africa
812 (<http://www.national.archives.gov.za/>), where they are kept in Archaeological Survey Files
813 (source ASW, volume 60, reference 20/1/A and B20/1/2A).

814 d'Errico, F., Backwell, L., Villa, P., Degano, I., Lucejko, J.J., Bamford, M.K., Higham, T., Colombini, M.P.,
815 Beaumont, P.B., 2012. Early evidence of San material culture represented by organic artifacts
816 from Border Cave, South Africa. *P. Natl. Acad. Sci. USA.* 109(33), 13214-13219.

817 de la Peña, P., Colino, F., d'Errico, F., Wadley, L., Banks, W., Stratford, D., Backwell, L., in press. Lithic
818 technological and spatial analysis of the final Pleistocene at Border Cave, South Africa.
819 *Quaternary Sci. Rev.*

820 Duller, G.A.T., 2003. Distinguishing quartz and feldspar in single grain luminescence measurements.
821 *Radiat. Meas.* 37, 161-165.

822 Duller, G.A.T., 2015. The Analyst software package for luminescence data: overview and recent
823 improvements. *Ancient TL* 33, 35-42.

824 Duller, G.A.T., 2012. Improving the accuracy and precision of equivalent doses determined using the
825 optically stimulated luminescence signal from single grains of quartz. *Radiat. Meas.* 47(9), 770-
826 777.

827 Durcan, J.A., Duller, G.A.T., 2011. The fast ratio: a rapid measure for testing the dominance of the fast
828 component in the initial OSL signal from quartz. *Radiat. Meas.* 46(10), 1065-1072.

829 Galbraith, R.F., Roberts, R.G., Laslett, G.M., Yoshida, H., Olley, J.M., 1999. Optical dating of single and
830 multiple grains of quartz from Jinmium rock shelter, northern Australia: Part I, experimental
831 design and statistical models. *Archaeometry* 41(2), 339-364.

832 Grün, R., Beaumont, P.B., 2001. Border Cave revisited: a revised ESR chronology. *J. Hum. Evol.* 40, 467-
833 482.

834 Grün, R., Beaumont, P.B., Stringer, C.B., 1990. Electron Spin Resonance ESR dating evidence for early
835 modern humans at Border Cave in South Africa. *Nature* 344 (6266), 537-539.

836 Grün, R., Beaumont, P., Tobias, P.V., Eggins, S., 2003. On the age of Border Cave 5 human mandible. *J.*
837 *Hum. Evol.* 45, 155-167.

838 Guérin, G., Mercier, N., Adamiec, G., 2011. Dose rate conversion factors: update. *Ancient TL* 29, 5-8.

839 Guérin, G., Mercier, N., Nathan, R., Adamiec, G., Lefrais, Y., 2012. On the use of the infinite matrix
840 assumption and associated concepts: A critical review. *Radiat. Meas.* 47, 778-85.

841 Hansen, V., Murray, A., Buylaert, J.P., Yeo, E.Y., Thomsen, K., 2015. A new irradiated quartz for beta
842 source calibration. *Radiat. Meas.* 81, 123-127.

843 Huntley, D.J., Baril, M.R., 1997. The K content of the K-feldspars being measured in optical dating or in
844 thermoluminescence dating. *Ancient TL* 15(1), 11-13.

845 Huntley, D.J., Hancock, R.G.V., 2001. The Rb contents of the K-feldspar grains being measured in optical
846 dating. *Ancient TL* 19(2), 43-46.

847 Jacobs, Z., Roberts, R.G., Galbraith, R.F., Deacon, H.J., Grün, R., Mackay, A., Mitchell, P., Vogelsang, R.,
848 Wadley, L., 2008. Ages for the Middle Stone Age of southern Africa: implications for human
849 behavior and dispersal. *Science* 322(5902), 733-735.

850 Jain, M., Murray, A.S., Bøtter-Jensen, L., 2003. Characterisation of blue-light stimulated luminescence
851 components in different quartz samples: implications for dose measurement. *Radiat. Meas.*
852 37(4-5), 441-449.

853 Kreutzer, S., Martin, L., Guérin, G., Tribolo, C., Selva, P., Mercier, N., 2018. Environmental dose rate
854 determination using a passive dosimeter: techniques and workflow for alpha-Al₂O₃: C chips.
855 *Geochronometria* 45, 56-67.

856 Kreutzer, S., Tribolo, C., Martin, L., Mercier, N., 2020. Dose-Rate Estimation using Al₂O₃: C chips:
857 Aftermath. *Ancient TL* 38, 1-10.

858 Lamothe, M., Brisson, L.F., Hardy, F., 2020. Circumvention of anomalous fading in feldspar
859 luminescence dating using Post-Isothermal IRSL. *Quat. Geochron.* 57, 101062.

860 Lamothe, M., Brisson, L. F., Hardy, F., 2018. Dose recovery performance in double IRSL/pIRIR SAR
861 protocols. *Radiat. Meas.* 120, 120-123.

862 Lanos, P., Dufresne, P., 2019. ChronoModel version 2.0 User manual. [https://hal.archives-
863 ouvertes.fr/hal-02058018](https://hal.archives-ouvertes.fr/hal-02058018)

864 Lanos, P. and Philippe, A. (2018). Event date model: a robust Bayesian tool for chronology building.
865 *Commun. for Stat. Applications and Meth.* 25(2):131-157.

866 Li, B., Roberts, R.G., Jacobs, Z., Li, S.H., Guo, Y.J., 2015. Construction of a 'global standardised growth
867 curve' (gSGC) for infrared stimulated luminescence dating of K-feldspar. *Quat. Geochron.* 27,
868 119-130.

869 Li, B., Jacobs, Z., Roberts, R. G., Galbraith, R., Peng, J., 2017. Variability in quartz OSL signals caused by
870 measurement uncertainties: Problems and solutions. *Quat. Geochron.* 41, 11-25.

871 Martin, L., 2015. Caractérisation et modélisation d'objets archéologiques en vue de leur datation par
872 des méthodes paléo-dosimétriques. Simulation des paramètres dosimétriques sous Geant4.
873 PhD thesis, University of Bordeaux Montaigne.

874 Mejdahl, V., Bøtter-Jensen, L., 1994. Luminescence dating of archaeological materials using a new
875 technique based on single aliquot measurements. *Quaternary Sci. Rev.* 13(5-7), 551-554.

876 Millard, A.R., 2006. Bayesian analysis of ESR dates, with application to Border Cave. *Quat. Geochron.*
877 1(2), 159-166.

878 Miller G.H., Beaumont P.B., 1989. Dating the Middle Stone Age at Border Cave, South Africa, by the
879 epimerization of the isoleucine in ostrich eggshells. *Bull. Geol. Soc. Am. Abstracts with programs*
880 21, A235.

881 Miller, G.H., Beaumont, P.B., Jull, A.J.T., Johnson, B., 1992. Pleistocene geochronology and the
882 paleothermometry from protein diagenesis in ostrich eggshells: implication for the evolution of
883 modern humans. Aitken M.J., Stringer C.B., and Mellars P.A. (eds.): The origin of modern Humans
884 and the impact of chronometric dating, 149-157. Philos. T. Roy. Soc. B.

885 Miller, G.H., Beaumont, P.B., Jull, A.J.T., Johnson, B., 1993. Pleistocene geochronology and the
886 paleothermometry from protein diagenesis in ostrich eggshells: implication for the evolution of
887 modern humans. In: Aitken, M.J., Stringer, C.B., and Mellars, P.A. (Eds.), The Origin of Modern
888 Humans and the Impact of Chronometric Dating. Princeton University Press, Princeton, pp. 49-
889 68.

890 Miller, G.H., Beaumont, P.B., Deacon, H.J., Brooks, A.S., Hare, P.E., Jull, A.J.T., 1999. Earliest modern
891 humans in southern Africa dated by isoleucine epimerization in ostrich eggshell. *Quaternary Sci.*
892 *Rev.* 18, 1537-1548.

893 Murray, A.S., Wintle, A.G., 2000. Luminescence dating of quartz using an improved single-aliquot
894 regenerative-dose protocol. *Radiat. Meas.* 32, 57-73.

895 Peng, J., Wang, X., Adamiec, G., 2022. The build-up of the laboratory-generated dose-response curve
896 and underestimation of equivalent dose for quartz OSL in the high dose region: A critical
897 modelling study. *Quat. Geochron.* 67, 101231.

898 Perić, Z.M., Marković, S.B., Filyó, D., Thiel, C., Murray, A.S., Gavrilov, M.B., Nett, J.J., Sipos, G., 2021.
899 Quartz OSL and polymineral post IR-IRSL dating of the Požarevac loess-palaeosol sequence in
900 north-eastern Serbia. *Quat. Geochron.* 66, 101216.

901 Philippe, A., Guérin, G., Kreutzer, S., 2019. BayLum-An R package for Bayesian analysis of OSL ages: An
902 introduction. *Quat. Geochron.* 49, 16-24.

903 Prescott, J.R., Hutton, J.T., 1994. Cosmic ray contributions to dose rates for luminescence and ESR
904 dating: large depths and long-term time variations. *Radiat. Meas.* 23, 497-500.

905 Rees-Jones, J., 1995. Optical dating of young sediments using fine-grain quartz. *Ancient TL* 13(2), 9-14.

906 Rhodes, E. J., Ramsey, C. B., Outram, Z., Batt, C., Willis, L., Dockrill, S., Bond, J., 2003. Bayesian methods
907 applied to the interpretation of multiple OSL dates: high precision sediment ages from Old
908 Scatness Broch excavations, Shetland Isles. *Quaternary Sci. Rev.* 22(10-13), 1231-1244.

909 Roberts, H. M., Duller, G.A., 2004. Standardised growth curves for optical dating of sediment using
910 multiple-grain aliquots. *Radiat. Meas.* 38(2), 241-252.

911 Sievers, C., Backwell, L., d'Errico, F., Wadley, L., 2022. Plant bedding construction between 60,000 and
912 40,000 years ago at Border Cave, South Africa. *Quaternary Sci. Rev.* 275: 107280.

913 Singhvi, A.K., Stokes, S.C., Chauhan, N., Nagar, Y.C., Jaiswal, M.K., 2011. Changes in natural OSL
914 sensitivity during single aliquot regeneration procedure and their implications for equivalent
915 dose determination. *Geochronometria* 38(3), 231-241.

916 Singhvi, A.K., Rajapara, H.M., Garnett, S., Chauhan, N., Gajjar, P.N., Wasson, R.J., 2021. How robust are
917 SAR single grain paleodoses: the role of sensitivity changes? LED 2021, 13-17th September 2021.
918 *Ancient TL* 39, S.

919 Steffen, D., Preusser, F., Schlunegger, F., 2009. OSL quartz age underestimation due to unstable signal
920 components. *Quat. Geochron.* 4(5), 353-362.

921 Stratford, D., Clark, J., Wojcieszak, M., de la Peña, P., Wadley, L., d'Errico, F., Mauran, G., Sievers, C.,
922 Banks, W., Beard, T., Horn, M., Shadrach, K., Morrissey, P., Backwell, L., 2022. Geoarchaeology
923 and zooarchaeology of Border Cave, South Africa: initial multiproxy considerations of
924 stratigraphy and site formation processes from the Backwell et al. excavations. *Quaternary Sci.*
925 *Rev.* 291: 107618.

926 Thomsen, K., Murray, A.S., Buylaert, J.P., Jain, M., Hansen, J.H., Aubry, T., 2016. Testing single-grain
927 quartz OSL methods using sediment samples with independent age control from the Bordes-
928 Fitte rockshelter (Roches d'Abilly site, Central France). *Quat. Geochron.* 31, 77-96.

929 Thomsen, K.J., Murray, A., Jain, M., 2012. The dose dependency of the over-dispersion of quartz OSL
930 single grain dose distributions. *Radiat. Meas.* 47(9), 732-739.

931 Tribolo, C., Mercier, N., Douville, E., Joron, J.-L., Reyss, J.-L., Rufer, D., Cantin, N., Lefrais, Y., Miller, C.E.,
932 Parkington, J., Porraz, G., Rigaud, J.-P., Texier, P.-J., 2013. OSL and TL dating of the Middle Stone

933 Age sequence of Diepkloof Rock Shelter (Western Cape, South Africa): a clarification. *J. Archaeol.*
934 *Sci.* 40 (9), 3401-3411.

935 Tribolo, C., Asrat, A., Bahain, J.-J., Chapon, C., Douville, E., Fragnol, C., Hernandez, M., Hovers, E.,
936 Leplongeon, A., Martin, L., Pleurdeau, D., Pearson, O., Puaud, S., Assefa, Z., 2017. When the
937 Rains Stopped: Geochronological and Sedimentological Evidence for the Middle and Later Stone
938 Age Sequence of Goda Buticha, Southeastern Ethiopia. *PlosOne* 12(1), e0169418.

939 Tsukamoto, S., Murray, A.S., Huot, S., Watanuki, T., Denby, P.M., Bøtter-Jensen, L., 2007. Luminescence
940 property of volcanic quartz and the use of red isothermal TL for dating tephtras. *Radiat. Meas.*
941 42(2), 190-197.

942 Villa, P., Soriano, S., Tsanova, T., Degano, I., Higham, T.F., d'Errico, F., Backwell, L.R., Lucejko, J.,
943 Beaumont, P.B., 2012. Border cave and the beginning of the Later Stone Age in South Africa. *P.*
944 *Natl. Acad. Sci. USA.* 109(33), 13208-13213.

945 Vogel, J.C., Beaumont, P.B., 1972. Revised radiocarbon chronology for the Stone Age in South Africa.
946 *Nature* 237(5349), 50-51.

947 Yoshida, H., Roberts, R.G., Olley, J.M., Laslett, G.M., Galbraith, R.F., 2000. Extending the age range of
948 optical dating using single 'supergrains' of quartz. *Radiat. Meas.* 32(5-6), 439-446.

949 Wadley, L., 2015. Those marvellous millennia: the Middle Stone Age of southern Africa. *Azania* 50(2),
950 155-226.

951

952

953 **Author contributions**

954 CT, NM, DS, LW, LB, FD conducted the sampling. CT, CD and NM conducted the luminescence dating
955 measurements. NC conducted the XRD analyses. WEB made the Bayesian modeling and calculations
956 and wrote the corresponding section. DS made Figure 1. CT wrote the manuscript. All authors
957 commented, corrected, and approved the final manuscript.

958

959 **Declaration of competing interest**

960 The authors declare that they have no competing financial interests or personal relationships that
961 could have influenced the work reported in this paper.

962

963